The primary nonlinear dynamics of modal and nonmodal perturbations of monochromatic inertia-gravity waves

Ulrich Achatz*

Leibniz-Institut für Atmosphärenphysik an der Universität Rostock

Kühlungsborn, Germany

*Leibniz-Institut für Atmosphärenphysik, Schloßstr. 6, 18225 Kühlungsborn, Germany, tel. +49-38293-68340, fax +49-38293-6850, e-mail achatz@iap-kborn.de

Abstract

The breaking of an inertia-gravity wave (IGW), initiated by its leading normal modes (NMs) or singular vectors (SVs), and the resulting small-scale eddies are investigated by means of direct numerical simulations of a Boussinesq fluid characterizing the upper mesosphere. The focus is on the primary nonlinear dynamics, neglecting the effect of secondary instabilities. It is found that the structures with the strongest impact on the IGW and also the largest turbulence amplitudes are the NM (for a statically unstable IGW) or short-term SV (statically and dynamically stable IGW) propagating horizontally transversely with respect to the IGW, possibly in agreement with observations of airglow ripples in conjunction with statically unstable IGWs. In both cases these leading structures reduce the IGW amplitude well below the static and dynamic instability thresholds. The resulting turbulent dissipation rates are within the range of available estimates from rocket soundings, even for IGWs at amplitudes low enough precluding NM instabilities. SVs thus can help explain turbulence occurring under conditions not amenable for the classic interpretation via static and dynamic instability. Due to an important role of the statically enhanced roll mechanism in the energy exchange between IGW and eddies the turbulent velocity fields are often conspicuously anisotropic. The spatial turbulence distribution is determined to a large degree by the elliptically polarized horizontal velocity field of the IGW.

1. Introduction

The importance of gravity waves for the dynamics of the middle atmosphere via their momentum and energy deposition has been known for a long time (Hines 1960; Houghton 1978; Lindzen 1981; Holton 1982, 1983; Garcia and Solomon 1985). In addition, turbulence with dissipation rates possibly of relevance for the mesospheric energy balance (Lübken 1997) might at least partially be traced back to gravity-wave breaking (Becker and Schmitz 2002). Since the major part of the corresponding wave spectrum is at scales which cannot be resolved within state-of-the-art general circulation models these can only incorporate gravity-wave effects via parameterizations. With this regard there are still considerable uncertainties since many details of (mostly tropospheric and stratospheric) gravity-wave radiation, propagation through the middle atmosphere, and breaking, predominantly in the mesosphere-lower-thermosphere (MLT), are not sufficiently understood yet (Fritts and Alexander 2003).

Numerical studies of the nonlinear breaking process, which is the focus of this paper, have traditionally resorted to some kind of large-eddy simulation (LES) with a flux-gradient type turbulence parameterization (Winters and D'Asaro 1994; Andreassen et al. 1994; Fritts et al. 1994; Isler et al. 1994; Lelong and Dunkerton 1998a,b). Direct numerical simulations (DNS) with their least ambiguous results on the corresponding turbulence dynamics have only recently become possible (Fritts et al. 2003, 2006). One might expect these to represent a useful laboratory for tests of gravity-wave parameterizations, but they are computationally still very expensive. So much the more interesting are linear studies yielding a-priori information about instability thresholds and the scales and structures of the most relevant initial perturbations in a breaking wave. While a DNS of wave breaking initialized by purely random perturbations sheds light on some aspects of the process, an alternative approach, equally interesting from the conceptual

point of view, is the study of the nonlinear development of a gravity wave after having been distinctly perturbed by its leading normal mode or another dynamically distinguished perturbation structure. Such studies can promote additional insight into the process by identifying its most paradigmatic features.

In this respect it seems appropriate to recognize that, roughly speaking, gravity waves fall under two main classes, differing in the importance of rotation for their dynamics. While high-frequency gravity waves (HGW) are mostly unaffected by the Coriolis force, inertia-gravity waves (IGWs), with nearly vertical phase propagation and periods of the order of the inertial period, exhibit an elliptic polarization of their velocity field which is a direct result of rotation. Correspondingly, their dynamics differ appreciably so that the breaking of these wave types should be studied separately. The present work represents an investigation of IGW breaking initialized by typical perturbations derived from linear theory.

Linear studies of modal IGW instability (Fritts and Yuan 1989; Yuan and Fritts 1989; Dunkerton 1997; Kwasniok and Schmitz 2003; Yau et al. 2004) have identified as basic parameters the ratio $R = |f/\omega|$ between inertial frequency and intrinsic wave frequency, the wave amplitude a with respect to static stability ($a = 1$ corresponding to the margin of static instability, i.e. local overturning of the contours of density or potential temperature), the Richardson number Ri at the statically least stable location, and the azimuthal angle α between the horizontal directions of propagation of a perturbation and the IGW. Neglecting the horizontal gradients in a monochromatic IGW one can derive from the inviscid-nondiffusive equations, after a Galilei transformation into the reference frame moving with the wave phase velocity, a modified Taylor-Goldstein equation of the type analyzed by Howard (1961) and Miles (1961). They have shown that a necessary condition for the existence of unstable normal modes (NMs)

in this equation is that there is a location where $\mathrm{Ri} < 1/4$. With certain restricting modifications (Lelong and Dunkerton 1998a, e.g.) this was also identified as a rough sufficient condition for NM instability. The NMs are preferentially parallel ($\alpha = 0$) for moderate R with not too steep an IGW wave vector, but more isotropic, i.e. with nearly equal amplification rate for transverse modes ($\alpha = 90°$), as $R \to 1$.

A limitation of these studies is their reliance on the existence of a reference frame within which the examined IGW is stationary, as is the case for a monochromatic wave, or, in view of the long period of an IGW, the simple neglect of its time dependence. Since stationarity of the examined reference solution (here the IGW) is a necessary condition for a NM analysis, a stability theory must be generalized to get rid of this limitation. This leads to the additional aspect that even for stationary reference states NM analyses only provide information about possible time-asymptotic wave instabilities at infinitely small perturbation level. It is however known from several other fields of fluid dynamics that under conditions when no growing NMs exist rapid transient growth of so-called optimal perturbations or singular vectors (SVs) can still be possible (Farrell 1988a,b; Boberg and Brosa 1988; Butler and Farrell 1992; Trefethen et al. 1993). Provided a sufficiently high, but possibly yet small initial perturbation level is available this can lead to the onset of turbulence even when such a result would not be expected from a NM analysis. Moreover, even if growing NMs exist, it may happen that they take much longer in their amplification so that the incipient instability is better characterized by transient growth leading directly into the nonlinear decay phase. Luckily, a SV analysis by which such possibilities are investigated does not rely on the stationarity of the wave examined. Motivated by such considerations, recent studies of optimal perturbations of IGWs (Achatz 2005; Achatz and Schmitz 2006a,b) have indeed shown that nonmodal transient perturbation growth by nearly

an order of magnitude in amplitude is possible for IGW amplitudes precluding unstable NMs. The propagation characteristics of the identified SVs are similar to that of NMs at larger a but they are typically more locally confined to the statically least stable location in the IGW, and they have shorter horizontal wavelengths.

While the linear dynamics of NMs and SVs of IGWs have thus been studied in some detail[1], their nonlinear development has not really been looked at yet in a DNS. Among the four studies coming nearest to this, Lelong and Dunkerton (1998a,b), on the one hand, have simulated IGW breaking in an LES without explicit treatment of the turbulent scales. With the intention of reducing the horizontal scale of the IGW for a given R they have also used a ratio f/N between inertial and Brunt-Vaisala frequency which exceeds typical values for the MLT by about an order of magnitude. Fritts et al. (2003, 2006), on the other hand, have treated either the case of HGW breaking or the instability of a simple shear layer, thus not including possible effects of the elliptic polarization of the IGW velocity field. The present study has the intent of going a step farther towards the simulation of the nonlinear development of an IGW perturbed by either a NM or a SV. Major points of interest are the change of the IGW amplitude, the energy exchange between IGW and perturbation, the distribution of perturbation energy between the various dynamical fields in question, its spatial distribution, and the strength and distribution of the occurring turbulent dissipation rates.

With this aim the paper is structured as follows: Section 2 describes the general setup of the model and the numerical experiments. Section 3 discusses a way of describing the energetics of the breaking process which facilitates an easier comparison with the previous linear studies. Section 4 gives an account of the simulations of a statically unstable IGW perturbed by a NM or

[1]A further interesting aspect not pursued here any further is the possible existence of packets of small-scale vortical perturbations growing due to a parametric resonance with the IGW (Miyazaki and Adachi 1998).

a SV, while section 5 discusses a statically and dynamically stable IGW ($a < 1$, $Ri > 1/4$, no NM instability) perturbed by one of its SVs. Section 6 compares the theory with some relevant observational findings, and section 7 gives a summary and discussion of the most important results.

2. Model setup

The equations used are the Boussinesq equations on an f plane, i.e.

$$\nabla \cdot \mathbf{v} = 0 \tag{1}$$

$$\frac{\partial \mathbf{v}}{\partial t} + (\mathbf{v} \cdot \nabla)\mathbf{v} + f\mathbf{e}_z \times \mathbf{v} + \nabla p - \mathbf{e}_z b = \nu \nabla^2 \mathbf{v} \tag{2}$$

$$\frac{\partial b}{\partial t} + (\mathbf{v} \cdot \nabla)b + N^2 w = \mu \nabla^2 b \quad . \tag{3}$$

Here $\mathbf{v} = (u, v, w)$ denotes the 3D velocity field. The buoyancy $b = g(\theta - \overline{\theta}(z))/\theta_0$ is a measure of the deviation of the potential temperature θ from a merely vertically dependent reference profile $\overline{\theta}(z)$, normalized by a characteristic value θ_0. g is the vertical gravitational acceleration. The squared background Brunt-Vaisala frequency is $N^2 = (g/\theta_0)d\overline{\theta}/dz$. An equivalent interpretation of buoyancy and Brunt-Vaisala frequency is $b = -g(\rho - \overline{\rho}(z))/\rho_0$ and $N^2 = -(g/\rho_0)d\overline{\rho}/dz$ where ρ, $\overline{\rho}(z)$, and ρ_0 are density, a corresponding reference field, and a characteristic value, respectively. p is the pressure field, normalized by a constant reference density, f the Coriolis parameter, and $\mathbf{e}_z$ the vertical unit vector. For viscosity and thermal diffusivity the typical upper-mesospheric values $\nu = \mu = 1\mathrm{m}^2/\mathrm{s}$ are taken. The f plane is located at 70° latitude. The Brunt-Vaisala frequency is $N = 2 \cdot 10^{-2}\mathrm{s}^{-1}$. For better readability for a broader audience it has been decided not to non-dimensionalize the equations. One should,

however, keep in mind that a non-dimensionalization, using the gravity-wave wavelength Λ (specified below) and the Brunt-Vaisala period $T = 2\pi/N$ as length and time scales, would leave as the only controlling parameters the ratio f/N, the Reynolds number $\mathrm{Re} = \Lambda^2/(\nu T)$, and the Prandtl number $\mathrm{Pr} = \nu/\mu$.

In the inviscid-nondiffusive limit the equations admit as exact solutions monochromatic gravity waves with wavenumber $\mathbf{k} = (k_x, k_y, k_z)$ and frequency ω satisfying the dispersion relation

$$\omega = \pm\sqrt{N^2 \cos^2\Theta + f^2 \sin^2\Theta} \qquad . \tag{4}$$

Here Θ is the inclination angle of the gravity-wave wave vector with respect to the horizontal so that $(\cos\Theta, \sin\Theta) = \left(k_x/\sqrt{k_x^2 + k_z^2}, k_z/\sqrt{k_x^2 + k_z^2}\right)$. Without loss of generality it is assumed that $k_y = 0$. At $k_z > 0$ the $-$-branch of the dispersion relation represents a wave with upward directed group velocity $\mathbf{c}_g = \nabla_{\mathbf{k}}\omega$, but downward directed phase velocity $\mathbf{c} = (\omega/k)\,(\mathbf{k}/k)$, where $k = |\mathbf{k}|$. Such a wave is examined in the present study. Following Mied (1976) and Drazin (1977) a coordinate system is introduced in which the representation of the gravity wave is especially simple. It is obtained by a rotation about the y-axis so that the new vertical coordinate points in the direction of the wavenumber vector, a translation along this axis with the phase velocity, and a rescaling of the vertical axis in units of the wave phase $\phi = \mathbf{k}\cdot\mathbf{x} - \omega t$ (see also Fig. 1). The new coordinates are (ξ, y, ϕ) with

$$(\xi, \phi) = [x\sin\Theta - z\cos\Theta, k\,(x\cos\Theta + z\sin\Theta) - \omega t] \tag{5}$$

The rotated velocity components along the new axes being u_ξ, v, and u_ϕ, the gravity wave takes

in this representation the time-independent form

$$(u_\xi, v, u_\phi, b)_{GW} = -ac\left(\frac{\sin\phi}{\sin\Theta\cos\Theta}, -\frac{f/\omega}{\cos\Theta}\cos\phi, 0, \frac{N^2/\omega}{\sin\Theta}\cos\phi\right) \quad , \tag{6}$$

where $c = \omega/k$. The phase convention (Yau et al. 2004) is such that the buoyancy gradient minimizes (maximizes) at $\phi = 3\pi/2$ $(\pi/2)$. The largest shear due to u_ξ occurs at $\phi = 0, \pi$, and the largest shear due to v is at the extrema of the buoyancy gradient. The nondimensional amplitude a is defined so that the wave is statically stable for $a < 1$, i.e. at these values one has $N^2 + \partial b/\partial z > 0$ everywhere.

In the stability analysis the equations have been linearized about the gravity-wave state (6). This has been done with viscosity and diffusion, but neglecting the weak IGW decay resulting from these. Abstractly denoting the perturbations by a state vector $\mathbf{x}$ (allowed to be complex), the linear model is then given by $d\mathbf{x}/dt = \mathcal{A}\mathbf{x}$ with some model operator $\mathcal{A}$. The corresponding NMs are simply defined as the eigenvectors $\mathbf{n}_\nu$ of the model operator, satisfying $\mathcal{A}\mathbf{n}_\nu = -i\left(\omega_\nu + i\gamma_\nu\right)\mathbf{n}_\nu$, with an eigenvalue consisting of an eigenfrequency ω_ν and a growth rate γ_ν. An initial state given up to an amplitude a_ν by a NM, i.e. $\mathbf{x}(0) = a_\nu\mathbf{n}_\nu$, leads in the linear limit to a time dependent solution $\mathbf{x}(t) = a_\nu e^{\gamma_\nu t}e^{i\omega_\nu t}\mathbf{n}_\nu$, so that the existence of a growing NM with $\gamma_\nu > 0$ implies linear instability. While a NM analysis thus searches perturbations growing exponentially in time, a SV analysis explores the possibility of rapid transient growth. Within the framework of a given norm $\|\mathbf{x}\|^2 = \overline{\mathbf{x}}^t\mathcal{M}\mathbf{x}$, here the energy norm defined by the appropriate metric $\mathcal{M}$, the SV analysis asks what initial perturbation $\mathbf{x}(0)$ would maximize for some given finite time τ the ratio $\|\mathbf{x}(\tau)\|^2 / \|\mathbf{x}(0)\|^2$. For an answer one needs the propagator matrix mapping the initial perturbation to its state at $t = \tau$ via $\mathbf{x}(\tau) = \mathbf{\Phi}(\tau)\mathbf{x}(0)$. Variational analysis tells us that the desired perturbation initializing strongest growth is the leading eigen-

vector $\mathbf{p}_\nu$ satisfying $\mathcal{M}^{-1}\overline{\mathbf{\Phi}}^t(\tau)\mathcal{M}\mathbf{\Phi}(\tau)\mathbf{p}_\nu = \sigma_\nu^2\mathbf{p}_\nu$ with the largest possible eigenvalue σ_ν^2, which is the squared growth factor $\|\mathbf{x}(\tau)\|^2 / \|\mathbf{x}(0)\|^2$ if $\mathbf{x}(0) = \mathbf{p}_\nu$. The time-dependent state $\mathbf{\Phi}(\tau)\mathbf{p}_\nu$ developing from an optimal perturbation $\mathbf{p}_\nu$ is the corresponding SV. Since the IGW is symmetric with respect to the "horizontal" directions ξ and y, one obtains here NMs and SVs for each combination of corresponding wave numbers. The resulting perturbations have the form $(\mathbf{v}', b') = \Re\left\{\left(\widehat{\mathbf{v}}, \widehat{b}\right)(\phi, t)\exp\left[i\left(\kappa\xi + \lambda y\right)\right]\right\}$ with $(\kappa, \lambda) = \frac{2\pi}{\lambda_\parallel}(\cos\alpha, \sin\alpha)$ being the horizontal wave-vector components. $\lambda_\parallel$ and α are the corresponding horizontal wavelength and the azimuthal angle between (κ, λ) and the ξ-axis. For details see eg. Achatz (2005).

In the simulations reported here the initial state for the nonlinear model is always obtained by a superposition of the gravity wave and the state of one of the linear NMs or SVs at $t = 0$. It is symmetric with respect to the direction in the $\xi - y$ plane transverse to the direction of propagation of the perturbation, and the model equations conserve this symmetry. It therefore makes sense to introduce a horizontally rotated system of coordinates

$$\left(x_\parallel, y_\perp\right) = \left(\xi\cos\alpha + y\sin\alpha, -\xi\sin\alpha + y\cos\alpha\right) \tag{7}$$

respectively pointing in the directions parallel and transverse to the direction of the horizontal wavenumber vector of the perturbation. In this representation the equation of continuity (1) stays formally the same while (2) and (3) are replaced by

$$\frac{Du_\parallel}{Dt} - f\left(\sin\Theta v_\perp - \sin\alpha\cos\Theta u_\phi\right) + \frac{\partial p}{\partial x_\parallel} + b\cos\alpha\cos\Theta = \nu\nabla^2 u_\parallel \tag{8}$$

$$\frac{Dv_\perp}{Dt} + f\left(\sin\Theta u_\parallel + \cos\alpha\cos\Theta u_\phi\right) + \frac{\partial p}{\partial y_\perp} - b\sin\alpha\cos\Theta = \nu\nabla^2 v_\perp \tag{9}$$

$$\frac{Du_\phi}{Dt} - f\left(\sin\alpha\cos\Theta u_\parallel + \cos\alpha\cos\Theta v_\perp\right) + k\frac{\partial p}{\partial\phi} - b\sin\Theta = \nu\nabla^2 u_\phi \tag{10}$$

$$\frac{Db}{Dt} + N^2 \underbrace{\left(-\cos\alpha\cos\Theta u_{\parallel} + \sin\alpha\cos\Theta v_{\perp} + \sin\Theta u_{\phi} \right)}_{w} \;=\; \mu\nabla^2 b \qquad , \qquad (11)$$

where $\left(u_{\parallel}, v_{\perp}\right)$ are the velocity components corresponding to $\left(x_{\parallel}, y_{\perp}\right)$, and $D/Dt = \partial/\partial t + v_{\parallel}\partial/\partial x_{\parallel} + v_{\perp}\partial/\partial y_{\perp} + (ku_{\phi} - \omega)\,\partial/\partial\phi$. This representation, up to the last rotation (7) identical to the one also used by Fritts et al. (2003, 2006), seems to be best suited for a study of the breaking of a monochromatic gravity wave, so that it provides the framework for the simulations reported here. Moreover, the periodicity of the initial conditions with respect to ϕ and $x_{\parallel}$ also implies a conservation of this property in the ensuing time development, so that the boundary conditions of the problem can be taken as periodic in all spatial directions.

For a numerical treatment the model equations have been discretized on a standard staggered C-grid, as discussed e.g. in Durran (1999), with periodic boundary conditions. The model domain extends from 0 to 2π in ϕ and 0 to $\lambda_{\parallel}$ in $x_{\parallel}$. Consistent with the here chosen initial states there is no dependence on $y_{\perp}$. The model might be called 2.5D since it describes buoyancy and a 3D velocity field depending on two spatial coordinates. Pressure is obtained by applying the divergence to the momentum equations and solving the resulting Poisson equation by a Fourier transform technique. The equations are integrated using a third-order Runge-Kutta time step (Durran 1999). The model resolution was always chosen fine enough to resolve both the inertial and the viscous subrange of the resulting turbulence spectra. Details are provided in table 1. It shall be stressed that the 2.5D approach with periodic boundary conditions, as convenient it might be for computational reasons, is also a desired simplification for better conceptual insight. Only with reference to the results from such an idealized study can more complex behavior, such as from local non-periodic initial perturbations or the full 3D behavior after secondary perturbations with a spatial dependence in $y_{\perp}$–direction, be understood most clearly.

3. Energetics

Since the basic IGW is horizontally symmetric (i.e. with respect to $x_\parallel$ and $y_\perp$) it seems helpful to analyze the interaction between IGW and perturbation in terms of the energy exchange between the horizontal mean $\left(\overline{\mathbf{v}}, \overline{b}\right)$ and the horizontally-dependent deviations $(\mathbf{v}', b') = (\mathbf{v}, b) - \left(\overline{\mathbf{v}}, \overline{b}\right)$ (for simplicity henceforth called "eddy" part). It is a standard procedure to derive from (1) and (8)–(11) the following budget equations for the kinetic energy densities $\overline{K} = \left|\overline{\mathbf{v}}\right|^2/2$ and $K' = \overline{\left|\mathbf{v}'\right|^2}/2$ and the densities of available potential energy $\overline{A} = \overline{b}^2/2N^2$ and $A' = \overline{b'^2}/2N^2$:

$$\frac{\partial \overline{K}}{\partial t} + k\frac{\partial}{\partial \phi}\left[\left(\overline{u}_\phi - c\right)\overline{K} + \overline{\mathbf{v}}\cdot\overline{u'_\phi \mathbf{v}'} + \overline{u}_\phi \overline{p} - \nu k \frac{\partial \overline{K}}{\partial \phi}\right] = \overline{w}\overline{b} - P_S - \overline{\epsilon} \tag{12}$$

$$\frac{\partial K'}{\partial t} + k\frac{\partial}{\partial \phi}\left[\left(\overline{u}_\phi - c\right)K' + \overline{u'_\phi \frac{\left|\mathbf{v}'\right|^2}{2}} + \overline{u'_\phi p'} - 2\nu\overline{v'_i S'_{i3}}\right] = \overline{w'b'} + P_S - \epsilon' \tag{13}$$

$$\frac{\partial \overline{A}}{\partial t} + k\frac{\partial}{\partial \phi}\left[\left(\overline{u}_\phi - c\right)\overline{A} + \frac{\overline{b}}{N^2}\overline{u'_\phi b'} - \mu k \frac{\partial \overline{A}}{\partial \phi}\right] = -\overline{w}\overline{b} - C - \overline{D} \tag{14}$$

$$\frac{\partial A'}{\partial t} + k\frac{\partial}{\partial \phi}\left[\left(\overline{u}_\phi - c\right)A' + \overline{u'_\phi \frac{b'^2}{2N^2}} - \mu k \frac{\partial A'}{\partial \phi}\right] = -\overline{w'b'} + C - D' \quad . \tag{15}$$

The contributing terms on the right-hand sides are shear production of eddy kinetic energy $P_S = -\overline{u'_\phi \mathbf{v}} \cdot \left(k\partial\overline{\mathbf{v}}/\partial\phi\right)$, convective production of eddy available potential energy $C = -\overline{u'_\phi b'}\left(k/N^2\right)\partial\overline{b}/\partial\phi$, dissipation of the horizontal-mean kinetic energy $\overline{\epsilon} = 2\nu\overline{S}_{ij}\overline{S}_{ij}$ (summing as usual over all double indices), eddy dissipation $\epsilon' = 2\nu\overline{S'_{ij}S'_{ij}}$, diffusive losses of horizontal-mean available potential energy $\overline{D} = \left(\mu/N^2\right)k^2\left|\partial\overline{b}/\partial\phi\right|^2$, and diffusive losses of the eddy available potential energy $D' = \left(\mu/N^2\right)\overline{\left|\nabla b'\right|^2}$. With the notations $(x_1, x_2, x_3) = \left(x_\parallel, y_\perp, \phi/k\right)$ and $(v_1, v_2, v_3) = \left(u_\parallel, v_\perp, u_\phi\right)$ the shear-stress tensors are defined as $\overline{S}_{ij} = \left(\partial\overline{v}_i/\partial x_j + \partial\overline{v}_j/\partial x_i\right)/2$ and $S'_{ij} = \left(\partial v'_i/\partial x_j + \partial v'_j/\partial x_i\right)/2$. The divergence terms on the left-hand sides of (12)–(15) serve to redistribute energy between different gravity-wave-phase locations, but they do not

contribute to the budget of the mean of all reservoirs in phase direction. In fact even many of the results below on the development of the $\phi-$dependence of the four energies can be understood without resorting to these terms. A graphic visualization of the energy cycle is given in figure 2. There $\langle\overline{K}\rangle$ denotes the mean of $\overline{K}$ over ϕ, and likewise for all other quantities.

From the definitions of P_S and C one can derive for the total eddy energy $E' = A' + K'$ the tendency $\partial\langle E'\rangle/\partial t = 2\Gamma\langle E'\rangle$ with an instantaneous amplification rate $\Gamma = \Gamma_\parallel + \Gamma_\perp + \Gamma_b + \Gamma_d$ where the amplification-rate parts

$$\begin{aligned}\left(\Gamma_\parallel, \Gamma_\perp, \Gamma_b, \Gamma_d\right) &= \langle\gamma_\parallel, \gamma_\perp, \gamma_b, \gamma_d\rangle \\ &= -\langle\overline{u'_\phi u'_\parallel}k\frac{\partial\overline{u}_\parallel}{\partial\phi}, \overline{u'_\phi v'_\perp}k\frac{\partial\overline{v}_\perp}{\partial\phi}, \overline{u'_\phi b'}\frac{k}{N^2}\frac{\partial\overline{b}}{\partial\phi}, D' + \epsilon'\rangle/2\langle E'\rangle \qquad , \quad (16)\end{aligned}$$

as in the linear dynamics (Achatz 2005), describe consecutively the impact of the eddy fluxes of momentum in $x_\parallel$- and $y_\perp$-direction against the corresponding gradients in the horizontal mean, as well as the effect of the counter-gradient buoyancy fluxes and of diffusive and viscous damping. The relative strengths of $\Gamma_\parallel$, $\Gamma_\perp$, and Γ_b tell us, in close analogy to the linear case, which part of the gain (or loss) of $\langle E'\rangle$ can be attributed to respective direct changes in $\langle K'_\parallel\rangle = \langle\overline{u'^2_\parallel}/2\rangle$, $\langle K'_\perp\rangle = \langle\overline{v'^2_\perp}/2\rangle$, and $\langle A'\rangle$. The respective contributions to $\overline{b'w'}/\langle 2E'\rangle$, i.e. $-\cos\alpha\cos\Theta\overline{u'_\parallel b'}/\langle 2E'\rangle$, $\sin\alpha\cos\Theta\overline{v'_\perp b'}/\langle 2E'\rangle$, and $\sin\Theta\overline{u'_\phi b'}/\langle 2E'\rangle$, indicate buoyant transfer from $\langle A'\rangle$ to $\langle K'_\parallel\rangle$, $\langle K'_\perp\rangle$, and $\langle K'_\phi\rangle = \langle\overline{u'^2_\phi}/2\rangle$. In the IGW case where $(\cos\Theta, \sin\Theta) \approx (0, 1)$ buoyant exchange occurs mainly between A' and $\langle K'_\phi\rangle \approx \langle\overline{w'^2}/2\rangle$.

4. NMs and SVs of a statically unstable IGW

The first set of experiments is meant to give an overview of the dynamics of modal and non-modal perturbations of statically unstable IGWs. For this an IGW is considered with $\Theta = 89.5°$ and $\Lambda = 2\pi/k = 6$km, so that $R = 0.62$. The IGW period is $P = 2\pi/\omega \approx 7.87\text{h} \approx 94\tau$. Its amplitude is $a = 1.2$. The linear dynamics of the NMs and SVs used as perturbations are described in Achatz (2005). The SVs exhibit optimal growth over an optimization time $\tau = 300$s, which is approximately one Brunt-Vaisala period $2\pi/N$. Among the multitude of possible NMs and SVs the leading structures at azimuthal angle $\alpha = 0, 90°$ were taken since they represent limit cases of the range of possible angles. In the linear limit NMs and SVs at intermediate azimuthal angles ($0° < \alpha < 90°$) show a kind of transitional behavior between these two. A choice had to be made concerning the perturbation amplitudes. The final decision was to choose an amplitude characterizing the peak strength of the energy density $e'\left(x_\parallel, \phi\right) = \left(u_\parallel'^2 + v_\perp'^2 + u_\phi'^2 + b'^2/N^2\right)/2$ in relation to the corresponding energy density of the IGW. From (6) one can see that the latter is uniform and identical to $\overline{E} = \overline{K} + \overline{A}$ at $t = 0$, which is $\overline{E}\,(t=0) = (a^2/2)\,c^2/\left(\sin\Theta\cos\Theta\right)^2$. In all cases reported here the initial ratio $\max_{x_\parallel,\phi}\left(e'\right)/\overline{E}$ is 10^{-3}, ensuring an initial behavior in agreement with linear theory.

Figure 3 shows the corresponding ratio $E'/\overline{E}$ at $t = 0$. While the three other perturbations are confined to the phase range near $\phi = 3\pi/2$, i.e. the statically most unstable region, the leading NM at $\alpha = 90°$ is quite smoothly spread over the whole range of IGW phases and, although it has the same peak energy as the other SVs and NM, its horizontal-mean energy E' is larger. As a consequence this pattern exhibits the largest fluxes and thus also the strongest interaction with the IGW. Figure 4 shows for all four integrations the decay in the energy in the horizontal mean. In the NM case at $\alpha = 90°$ the energy seems to already approach by $t = 2P$

an asymptotic limit near $0.4\overline{E}(t=0)$, while the other three cases show a much slower decay. This has to be put into contrast with the growth factors the four patterns have according to the linear theory between $t=0$ and $t=\tau$, where the NM at $\alpha=90^\circ$ shows the least vigorous behavior.

An interesting feature in the development of the contributions to the eddy energy, i.e. $\langle K'_\perp\rangle$, $\langle K'_\parallel\rangle$, $\langle K'_\phi\rangle$, and $\langle A'\rangle$ (not shown), is that in all cases but the one of the NM at $\alpha=90^\circ$ the dominating term is $\langle K'_\perp\rangle$. This is consistent with the time dependence of the amplification-rate decomposition shown in Fig. 5 for $0\le t\le 10\tau$. For the three cases one sees the later phase to be dominated by a balance between energy gain due to the counter-gradient flux of $v_\perp$ and viscous-diffusive losses. This is in agreement with predictions from the linear theory where the corresponding statically enhanced roll mechanism always shows up as a strong energy source (Moffat 1967; Ellingsen and Palm 1975; Landahl 1980; Farrell and Ioannou 1993; Bakas et al. 2001; Achatz and Schmitz 2006a,b; Achatz 2005). A further agreement with the linear theory is visible in the energetics for $0\le t\le\tau$ where the transient behavior with strong peak amplification rates is visible for the SVs, and a nearly constant amplification-rate decomposition for the NMs. Also the details agree with those predictions: Initially the growth of both SVs is triggered by buoyant exchange, later followed by growth due to $\Gamma_\perp$ (statically enhanced roll mechanism) for $\alpha=0^\circ$ and growth due to $\Gamma_\parallel$ for $\alpha=90^\circ$, as in a statically enhanced Orr mechanism (Orr 1907; Farrell and Ioannou 1993; Bakas et al. 2001; Achatz and Schmitz 2006a,b). In the latter case finally the roll mechanism also takes over.

4a. *Parallel modes ($\alpha = 0°$)*

Consistent with the initial distribution (Fig. 3) the eddy energy density in the two cases for $\alpha = 0°$ (left column of Fig. 6) stays more or less confined to the most unstable phase range, while splitting up into two peaks which are gradually moving away from $\phi = 3\pi/2$. The mechanism behind this is illustrated for the SV at $\alpha = 0°$ in Fig. 7. One sees there $\gamma_\perp$ and its two contributors, i.e. the counter-gradient flux $-\overline{u'_\phi v'_\perp}$ and $\overline{v}_\perp$ (the latter entering into $\gamma_\perp$ via its phase gradient). One sees that by $t = \tau$ the fluxes have reversed the gradient of the horizontal mean, leading to a damping of the perturbation in the innermost part of the active region. The reversal of the internal gradient, however, has also led to an increased gradient at the edges of the active region, so that there the perturbation can continue to grow. By $t = 1.2\tau$ it has thus led to small subregions on the internal side of the edges of the active regions where the same repeats itself on a smaller scale. At the same time the momentum fluxes, damped in the internal region, but further excited on the outside, push the increased gradients at the edges farther out. This process continues, and thus leads to the energy-density distribution observed in Fig. 6. At a later phase the fluxes have reduced the gradients in $\overline{v}_\perp$ enough so that the growth in eddy energy is stalled. Even later, however, it bursts up again (near $t = 9\tau$, e.g.). A closer analysis can explain this in terms of partially reorganized gradients $\partial\overline{v}_\perp/\partial\phi$ allowing stronger transient (i.e. optimal) growth of perturbations there (not shown). The NM at $\alpha = 0°$ turns out to be similar in behavior.

4b. *Transverse modes ($\alpha = 90°$)*

As already in its linear dynamics the SV at $\alpha = 90°$ shows in its early development phase behavior as in a statically enhanced Orr mechanism, where a combination of static instability and counter-gradient fluxes of $u_\parallel$ in the statically most unstable phase region triggers its growth. Later the perturbations radiate away into regions where the $\partial\overline{v}_\perp/\partial\phi \neq 0$ (see Fig. 6). As visible in Fig. 8, there a roll mechanism takes over and further amplifies the perturbation by the action of counter-gradient fluxes in $v_\perp$. Also here edges of increased gradients $k\partial\overline{v}_\perp/\partial\phi$ form where the perturbation can experience further transient growth. Roughly between $t = \tau$ and $t = 5\tau$ one sees the fluxes $\overline{u'_\phi v'_\perp}$ oscillating about a zero mean. This is consistent with a roll mechanism without feedback on the horizontal mean (Achatz and Schmitz 2006a,b). Seemingly in this phase the impact on $\overline{v}_\perp$ is not strong enough to prevent this oscillation which later, at least at the lower edge, dies down in favor of a permanently positive $\gamma_\perp$. In the linear dynamics that mode also shows a critical-layer behavior near $\phi = \pi/2$. Although weakly discernible, it is not that important a process in the nonlinear development of the SV at the given initial amplitude.

At equal peak energy density the most vigorous, but also the most complex mode is the NM at $\alpha = 90°$. This one is somewhat less dominated by the statically enhanced roll mechanism than the others. Figure 9 shows for $0 \leq t \leq P/2$ the time and phase dependence of the four contributing eddy energy densities, while Fig. 6 shows the total. Still, however, much of the eddy energy is in $v'_\perp$ which maximizes near $\phi = \pi$. This is the region where for $\alpha = 90°$ the gradient $\partial\overline{v}_\perp/\partial\phi$ in the original IGW is largest, so indeed also here one seems to see the roll mechanism at work. Another important term is the eddy available potential energy A' which gets large near $\phi = \pi/2$. This seems to be a case of a critical-layer interaction similar to the one found in the linear dynamics of the leading SV at $\alpha = 90°$ (Achatz 2005; Achatz and Schmitz

2006a,b). This is further borne out by a comparison of the divergence terms in (15) with $\partial A'/\partial t$ which exhibit a considerable resemblance (also not shown), indicating that radiation and thus nonlocal effects seem to play a role here.

5. SVs of a statically and dynamically stable IGW

The second set of experiments addresses the nonlinear dynamics of SVs for an IGW amplitude ($a = 0.87$) precluding the existence of unstable NMs. Achatz (2005) describes the linear dynamics of these SVs for an IGW with again $\Theta = 89.5°$ and $\Lambda = 2\pi/k = 6$km (so that $R = 0.62$). It is shown that at an optimization time $\tau = 5$min the most strongly growing SV is at $\alpha = 0°$, with a growth factor near 10, while the so-called global optimal, i.e. the most strongly growing SV for all optimization times, is found to be the SV for $(\tau, \alpha) = (30\mathrm{min}, 90°)$, with a growth factor near 20. Based on these results the present study discusses integrations of the IGW after a perturbation by its leading SVs at $\tau = 5$min and 30min, and $\alpha = 0°$ and $90°$. Given the finite growth factors one expects a purely linear behavior of these at very small initial amplitude but possibly nonlinear dynamics with feedback on the IGW at larger initial amplitude. For an overview integrations have been done with ratios between initial peak energy density and IGW energy density $A^2_{\mathrm{SV}} = \max_{x_\parallel,\phi}(e')/\overline{E} = 10^{-2}, 10^{-1}$, and 10^0.

For $A^2_{\mathrm{SV}} = 10^{-1}$ the initial horizontal-mean energy density E' (normalized by $\overline{E}$) of the SVs is shown in Fig. 10. As one sees they are all located near $\phi = 3\pi/2$. The broadest and most energetic structure is the SV for $(\tau, \alpha) = (5\mathrm{min}, 90°)$. Consistent with this, that SV has the strongest effect on the IGW. Figs. 11 and 12 show the time dependence of $\langle E' \rangle$ and $\langle \overline{E} \rangle$ for all integrations. One sees that larger A^2_{SV} imply a stronger decay in $\langle \overline{E} \rangle$, which can go as far as by a factor 0.75, for the case of the SV for $(\tau, \alpha) = (5\mathrm{min}, 90°)$ with an initial amplitude

$A^2_{SV} = 10^0$. That case also shows a sustained initial rise of $\langle E' \rangle$ indicating linear behavior. For the other SVs such a strong initial amplitude leads, however, rather quickly to a decay of the eddy energy, showing that for these cases the initial SV amplitude is too large to allow an initial dynamics in agreement with the linear theory. One also sees that the initial growth phase gets longer as the initial SV amplitude is decreased, since larger initial eddy energy leads to an earlier impact of nonlinearity. Finally, as a major difference to the case of the statically unstable IGW, the development is more rapid in the sense that the eddies have no more than two optimization periods time to interact with the IGW before their energy decays again.

The amplification-rate decompositions for the four integrations with initial $A^2_{\rm SV} = 10^{-1}$ are shown in Fig. 13. The initial development is as in the linear theory, with an initial energy gain due to Γ_b, leading via $\overline{b'w'}$ to a growing energy in u'_ϕ, thus enabling a statically enhanced roll mechanism for $\alpha = 0^\circ$ (i.e. growth of $\langle K'_\perp \rangle$ via $\Gamma_\perp$) and a statically enhanced Orr mechanism for $\alpha = 90^\circ$ (growth of $\langle K'_\parallel \rangle$ via $\Gamma_\parallel$). In the case of $(\tau, \alpha) = (5\mathrm{min}, 90^\circ)$ in the late phase $\langle K'_\perp \rangle$ gains by the same mechanism as described above for $a = 1.2$, but in the case of $\tau = 30$min this is blocked by a rapid decrease of the amplification rate around $t = 0.3\tau$, an effect which is also visible in the two cases for $\alpha = 0^\circ$. Seemingly, nonlinear interactions stall any further growth of the eddy energy to be expected from the linear theory. This is followed by a rise of viscous-diffusive damping indicating an increased role from turbulent dissipation. The spatial distribution of the eddy energy is shown in Fig. 14.

5a. *Short optimization time $\tau = 5$min*

From the two SV cases for $\tau = 5$min the one for $\alpha = 0^\circ$ is less spectacular. Closer inspection shows its initial dynamics to be quite relate to the corresponding case discussed above for $a =$

1.2, with the same leading contribution from $K'_\perp$ (not shown). As seen from Fig. 15, the SV for $\alpha = 90°$ also shows behavior relate to the corresponding structure for $a = 1.2$, however with a stronger contribution from the statically enhanced Orr process which shall be shortly illustrated here. First comes a decrease in A'. As visible in Fig. 16, this results from a contribution $\gamma_b > 0$ in the statically least stable region, which for $a < 1$ automatically leads to a contribution $\gamma_b - \overline{b'w'}/\langle 2E' \rangle < 0$ there so that the eddy energy ends up in K'_ϕ (Achatz and Schmitz 2006a,b). As in the classic Orr process this swings back after some time, here followed by a second similar oscillation with opposite tendencies in A' and K'_ϕ. Accompanying this is an enhanced counter-gradient flux of $u'_\parallel$ (Fig. 17), leading to transient growth of $K'_\parallel$. As visible in Fig. 17, the effect of the eddies is to invert the gradient $k\partial\overline{u}_\parallel/\partial\phi$ near $\phi = 3\pi/2$, thus weakening the further growth of $K'_\parallel$. Simultaneously the gradient is increased at the outer edges, so that there an enhanced eddy growth is possible. Similar to the classic Orr process, growth in eddy energy is stopped near $t = \tau$, followed by a decay and a weaker second oscillation of a similar kind, after which the horizontal mean shows an increasingly turbulent structure. Also here, however, the gain in $K'_\perp$ is considerable, once again after the eddies have radiated outwards into regions where $\partial\overline{v}_\perp/\partial\phi \neq 0$. Another feature visible here in the later phase is an accumulation of A' near $\phi = \pi/2$, which is a visible consequence of the critical-layer interaction predicted by the linear theory (see Fig. 15).

An interesting question is why the leading transverse SV can follow its linear development for a longer time, so that even for $A^2_{\mathrm{SV}} = 1$ a corresponding phase is observable. At least part of the answer can be read from Fig. 18 where the time development of $v_\perp$ up to $t = \tau/2$ is shown for the parallel ($\alpha = 0°$) and the transverse SV ($\alpha = 90°$). One sees the parallel SV developing considerably stronger gradients (note that $\lambda_\parallel$ for the parallel SV is also shorter

than for the transverse SV), which can lead both to faster viscous damping and to stronger instabilities. Indeed corresponding calculations have shown that the parallel SV in its early stage allows stronger tangent linear instabilities than the other structure, so that it cannot go unimpeded through its full linear growth phase, while the opposite is true for the transverse SV (not shown).

5b. *Long optimization time* $\tau = 30$*min*

As much in contrast to the linear theory as the stronger growth of transverse SV vs. parallel SV for small τ is the second result that overall the SVs for longer τ cannot grow considerably in eddy energy. Indeed, due to its larger initial energy the leading parallel SV for $\tau = 30$min has some impact on the IGW, which is however weaker than that of the leading transverse SV for $\tau = 5$min. The early development of $v_\perp$ for the two SVs analyzed here is shown in Fig. 19. In comparison to Fig. 18 one sees at the same t/τ a stronger impact from the nonlinear advection, which already explains the reduced ability of the SVs to go unimpeded through their whole linear growth. It is just the fact that τ is larger but the nonlinear interactions are not correspondingly smaller and thus act faster over the normalized time t/τ which keeps these SVs from attaining the full energy they would acquire according to the linear theory.

6. Comparison to observations

A detailed comparison of the breaking of a monochromatic IGW in a background without vertical shear, as discussed here, with observations where these conditions are never met in purity, will probably never be possible. Nonetheless an attempt shall be made to point out a few obser-

vational facts indicating at least some consistency between the theory and the real world. Some of these refer to observations of so-called ripples in the airglow layer, which are commonly interpreted as instability structures from GW breaking (Hecht 2004). The literature seems to indicate that in cases where ripples are observed simultaneously with a statically unstable IGW (Hecht et al. 1997, 2000) they have a tendency to propagate in a more or less transverse horizontal direction with respect to the IGW. The wavelength of these structures is below 10km. A simulation of ripples from a statically unstable IGW has been done by Fritts et al. (1997), where the IGW (plus an additional HGW) has been perturbed by random noise. The results here, where the leading transverse NM appears as the most effective perturbation of an IGW with $a > 1$, might give an explanation for why the occurring ripples have the observed direction of propagation. Additional support for this hypothesis might come from the wavelength of the NM (about 8km) which is consistent with the empirical results.

Another point of interest are estimates of turbulent dissipation rates where spectra of vertical profiles of relative density fluctuations from in-situ rocket measurements are fitted to models of the spectrum of a passive tracer advected in homogeneous isotropic turbulence. Essentially the location of the transition from the inertial to the viscous subrange of the spectrum is then used to determine the dissipation rate. These analyses (Lübken 1997; Müllemann et al. 2003) lead to values of ϵ in the middle atmosphere between 1 and 1000mW/kg. Interesting is also that not in all cases turbulence can be clearly attributed to either static or dynamic instability. The long-term development of the eddy dissipation rates ϵ' resulting from the above-discussed integrations for the statically unstable IGW is shown in Fig. 20. The dissipation $\bar{\epsilon}$ of the horizontal mean is found to be much weaker (not shown). One sees that the former are in all four cases in the range of observed values. The eddy dissipation rates from developing SVs

of the statically and dynamically stable IGW are shown in Figs. 21 and 22. While most SVs produce values of a few 10 mW/kg, the leading transverse SV for the short optimization time can lead to dissipation rates of a few 100 mW/kg, provided its initial amplitude is large enough. SVs thus seem to offer a possibility to explain the occurrence of turbulence in cases where neither static nor dynamic instability predict corresponding NM growth[2]. Also here, however, a caveat applies. Fig. 23 shows the horizontally averaged spectra of the vertical profiles (i.e. in ϕ-direction) of all four model variables at $t = 40\tau$ from the integrations of the IGW with $a = 1.2$ and its leading parallel or transverse SV or NM. The dominance of $K'_\perp$ noted before obviously extends down into the viscous subrange, and also at all scales $u_\parallel$ carries more energy than u_ϕ. Similar results are found for the cases with $a = 0.87$ (not shown). This anisotropy might point to either (1) a limitation of the 2.5D approach taken here or (2) a fundamental property of turbulence from IGW breaking. A corresponding analysis is beyond the scope of this paper but at the present stage one should at least keep this apparent inconsistency with the basic assumptions behind the retrieval of turbulent dissipation rates from the spectra of density fluctuations in mind. Nonetheless, the author sees the agreement in the orders of magnitude between empirical and theoretical dissipation rates still as an indication of consistency between theory and measurements.

7. Summary and discussion

As a step towards the construction of a comprehensive picture of the nonlinear development of monochromatic inertia-gravity waves (IGWs) after being perturbed by their leading normal

[2]In passing it shall also be noted that the spatial distribution of ϵ' for the short-time transverse SV results from the action of the roll mechanism at the flanks of the maximum of $v_\perp$, an effect not to be expected in turbulence generated by a Kelvin-Helmholtz layer. It is also interesting that it stays clearly away from the phase region $\phi = \pi/2$ which can be explained via the critical-layer effect predicted by the linear theory

modes (NMs) or singular vectors (SVs) the present study reports corresponding direct numerical simulations for IGWs which are either statically unstable (amplitude a with respect to the overturning threshold larger than 1) or dynamically and statically stable ($a < 1$, $\mathrm{Ri} > 1/4$, no NM instabilities). The two spatial dimensions of the problem are given by the direction along the IGW wave vector and the horizontal wave vector of the perturbation, while the velocity field, simulated together with the buoyancy field within the framework of the nonlinear Boussinesq equations, is fully 3D. The model parameters are typical for the upper mesosphere.

An interesting aspect of the results is how much of the observed dynamics can be understood based on the corresponding linear theory (Achatz 2005; Achatz and Schmitz 2006a,b). An especially prominent role in the turbulence onset can be attributed to the statically enhanced roll mechanism, where the counter-gradient flux (i.e. against the corresponding gradient in the horizontal mean) of the eddy horizontal velocity component $v'_\perp$, in the direction perpendicular to the horizontal direction of propagation of the perturbation, leads to a corresponding gain in the eddy kinetic energy, thus producing a considerable anisotropy in the turbulent velocity field. This must be seen in connection with the role of the elliptic polarization of the IGW horizontal velocity field. It provides the key for understanding the spatial distribution of the eddy energy and turbulent dissipation with respect to the wave phase. This refers on the one hand to its role in determining where the roll mechanism can work. On the other hand it also leads to critical layers for the transverse perturbations (azimuthal angle between the horizontal direction of propagation of the perturbation with respect to that of the IGW $\alpha = 90°$), half a wavelength away from the statically least stable location, which the flux of turbulent energy typically does not cross. The present study thus adds interesting facets to the results from studies on turbulence onset via Kelvin-Helmholtz instabilities (with a one-dimensional shear) where these phenomena

are not visible.

In contrast to expectations from the linear theory, in the case of the statically and dynamically stable IGW the leading SVs for longer optimization times ($\tau = 30$min) are not able to grow to the largest observed eddy energies since, at initial SV amplitudes large enough for triggering nonlinear behavior, nonlinear advection acts too fast for allowing the perturbation to go through its full linear growth phase. In a comparison between the impact of the remaining leading parallel ($\alpha = 0°$) or transverse short-time SVs (for $\tau = 5$min) or NMs (for $a > 1$) on the IGW the overall finding is that, at equal local peak energy density, the more vigorous effect comes from the spatially broadest structure (in IGW-phase direction), which is the leading transverse NM for $a > 1$ and the leading transverse SV for $a < 1$ and $\mathrm{Ri} > 1/4$. These structures, with horizontal wavelengths roughly of the order of the total wavelength of the IGW, are the most energetic and thus have the largest eddy fluxes with a corresponding effect on the horizontal mean. They might help explain the wavelengths and preferentially more or less transverse orientation of airglow ripples typically observed in conjunction with a statically unstable IGW (Hecht et al. 1997, 2000).

One should also note that the reduction of the horizontal-mean energy, the square root of which gives an upper limit of the reduction of IGW amplitude, is stronger than to be expected from standard static or dynamic stability considerations. So it is found that the energy in the statically unstable IGW is reduced by a factor near 0.4, although removal of dynamically unstable regions with $\mathrm{Ri} < 1/4$ would only necessitate a reduction of a by a factor 0.7 (e.g. see Fig. 2 in Achatz, 2005) and correspondingly of the energy by a factor 0.5. Likewise, a reduction of the horizontal-mean energy by a factor less than 0.8 is also possible for $a = 0.87$, although this case precludes static or dynamic NM instabilities. This depends on the initial strength of

the perturbation which is not taken into account in standard parameterization schemes for the impact of gravity waves on the large-scale circulation.

The resulting turbulent dissipation rates are in all cases examined within the range of values determined from the spectra of vertical density fluctuation profiles (Lübken 1997; Müllemann et al. 2003), even for the case $a = 0.87$. Optimal perturbations thus indeed seem to be a candidate for the explanation of turbulence onset in IGWs where the wave amplitude precludes NM instabilities. A major difference between statically unstable and stable IGWs is that the turbulence in the latter occurs in rather short bursts over a time span of a few Brunt-Vaisala periods $2\pi/N$, while in the former the turbulent layer is much more persistent.

Finally, what have we learned so far which might be relevant for parameterizations? Perhaps the most important message is that wave breaking can set in earlier, and that a GW can deposit more of its momentum than typically assumed nowadays. Partly this was already clear from the previous linear NM theory of HGW instability (Mied 1976; Klostermeyer 1982, 1983, 1991; Lombard and Riley 1996; Sonmor and Klaassen 1997) and corresponding 3D DNS by Fritts et al. (2003, 2006), but it is supplemented by the additional option of IGW decay due to the impact of nonmodal perturbations, and as a whole none of these findings has yet found its way into a parameterization scheme. Unfortunately, a major problem remaining is the question as to whether it is possible to understand and predict the final amplitude of the GW. Next to the GW properties, this also seems to be sensitively dependent on the specific initial perturbations and their strength. Much work remains to be done here. It shall also be remarked that to all expectations the present results will be subject to modifications once the effect of secondary instabilities is taken into account, probably leading to a full three-dimensionalization of the turbulent fields (Klaassen and Peltier 1985; Winters and D'Asaro 1994; Andreassen et al. 1994).

Among other aspects it will be interesting how much of the spectral anisotropy found here will also be obtained under such conditions. Corresponding studies will have to be done in the future, for which the present one shall then serve as a reference.

Acknowledgement The author gratefully acknowledges discussions with G. Schmitz and M. Rapp, and the comments from three anonymous reviewers, which helped in improving the manuscript.

References

Achatz, U., 2005: On the role of optimal perturbations in the instability of monochromatic gravity waves. *Phys. Fluids*, **17**, 094107 1–27.

Achatz, U. and G. Schmitz, 2006a: Shear and static instability of inertia-gravity wave packets: Short-term modal and nonmodal growth. *J. Atmos. Sci.*, **63**, 397–413.

— 2006b: Optimal growth in inertia-gravity wave packets: Energetics, long-term development, and three-dimensional structure. *J. Atmos. Sci.*, **63**, 414–434.

Andreassen, Ø., C. E. Wasberg, D. C. Fritts, and J. R. Isler, 1994: Gravity wave breaking in two and three dimensions. 1. Model description and comparison of two-dimensional evolutions. *J. Geophys. Res.*, **99**, 8095–8108.

Bakas, N. A., P. J. Ioannou, and G. E. Kefaliakos, 2001: The emergence of coherent structures in stratified shear flow. *J. Atmos. Sci.*, **58**, 2790–2806.

Becker, E. and G. Schmitz, 2002: Energy deposition and turbulent dissipation owing to gravity waves in the mesosphere. *J. Atmos. Sci.*, **59**, 54–68.

Boberg, L. and U. Brosa, 1988: Onset of turbulence in a pipe. *Z. Naturforschung*, **43A**, 697–726.

Butler, K. M. and B. F. Farrell, 1992: Three dimensional optimal perturbations in viscous shear flow. *Phys. Fluids A*, **4**, 1637–1650.

Drazin, P. G., 1977: On the instability of an internal gravity wave. *Proc. R. Soc. London A*, **356**, 411–432.

Dunkerton, T. J., 1997: Shear instability of internal inertia-gravity waves. *J. Atmos. Sci.*, **54**, 1628–1641.

Durran, D. R., 1999: *Numerical methods for wave equations in geophysical fluid dynamics*. Springer, New York.

Ellingsen, T. and E. Palm, 1975: Stability of linear flow. *Phys. Fluids*, **18**, 487–488.

Farrell, B. F., 1988a: Optimal excitation of neutral rossby waves. *J. Atmos. Sci.*, **45**, 163–172.

— 1988b: Optimal excitation of perturbations in viscous shear flow. *Phys. Fluids*, **31**, 2093–2102.

Farrell, B. F. and P. J. Ioannou, 1993: Transient development of perturbations in stratified shear flow. *J. Atmos. Sci.*, **50**, 2201–2214.

Fritts, D. C. and M. J. Alexander, 2003: Gravity wave dynamics and effects in the middle atmosphere. *Rev. Geophys.*, **41**, 1003, doi:10.1029/2001RG000106.

Fritts, D. C., C. Bizon, J. A. Werne, and C. K. Meyer, 2003: Layering accompanying turbulence generation due to shear instability and gravity-wave breaking. *J. Geophys. Res.*, **108**, 8452, doi:10.1029/2002JD002406.

Fritts, D. C., J. R. Isler, and Ø. Andreassen, 1994: Gravity wave breaking in two and three dimensions. 2. Three-dimensional evolution and instability structure. *J. Geophys. Res.*, **99**, 8109–8124.

Fritts, D. C., J. R. Isler, J. H. Hecht, R. L. Walterscheid, and Ø. Andreassen, 1997: Wave breaking signatures in sodium densities and OH nightglow. 2. Simulation of wave and instability structures. *J. Geophys. Res.*, **102**, 6669–6684.

Fritts, D. C., S. L. Vadas, K. Wan, and J. A. Werne, 2006: Mean and variable forcing of the middle atmosphere by gravity waves. *J. Atmos. Sol.-Terr. Phys.*, **68**, 247–265.

Fritts, D. C. and L. Yuan, 1989: Stability analysis of inertio-gravity wave structure in the middle atmosphere. *J. Atmos. Sci.*, **46**, 1738–1745.

Garcia, R. R. and S. Solomon, 1985: The effect of breaking gravity waves on the dynamics and chemical composition of the mesosphere and lower thermosphere. *J. Geophys. Res.*, **90**, 3850–3868.

Hecht, J. H., 2004: Instability layers and airglow imaging. *Rev. Geophys.*, **42**, RG1001, doi:10.1029/2003RG000131.

Hecht, J. H., C. Fricke-Begemann, R. L. Walterscheid, and J. Höffner, 2000: Observations of the breakdown of an atmospheric gravity wave near the cold summer mesopause at 54N. *Geophys. Res. Lett.*, **27**, 879–882.

Hecht, J. H., R. L. Walterscheid, D. C. Fritts, J. R. Isler, D. C. Senft, C. S. Gardner, and J. S. Franke, 1997: Wave breaking signatures in OH airglow and sodium densities and temperatures. 1. Airglow imaging, Na lidar, and MF radar observations. *J. Geophys. Res.*, **102**, 6655–6668.

Hines, C. O., 1960: Internal atmospheric gravity waves at ionospheric heights. *Can. J. Phys.*, **38**, 1441–1481.

Holton, J. R., 1982: The role of gravity wave induced drag and diffusion in the momentum budget of the mesosphere. *J. Atmos. Sci.*, **39**, 791–799.

— 1983: The influence of gravity wave breaking on the general circulation of the middle atmosphere. *J. Atmos. Sci.*, **40**, 2497–2507.

Houghton, J. T., 1978: The stratosphere and mesosphere. *Q. J. R. Meteorol. Soc*, **104**, 1–29.

Howard, L., 1961: Note on a paper of John W. Miles. *J. Fluid Mech.*, **10**, 509–512.

Isler, J. R., D. C. Fritts, Ø. Andreassen, and C. E. Wasberg, 1994: Gravity wave breaking in two and three dimensions. 3. Vortex breakdown and transition to isotropy. *J. Geophys. Res.*, **99**, 8125–8138.

Klaassen, G. P. and W. R. Peltier, 1985: The onset of turbulence in finite-amplitude Kelvin-Helmholtz billows. *J. Fluid Mech.*, **155**, 1–35.

Klostermeyer, J., 1982: On parametric instabilities of finite-amplitude internal gravity waves. *J. Fluid Mech.*, **119**, 367–377.

— 1983: Parametric instabilities of internal gravity waves in Boussinesq fluids with large Reynolds numbers. *Geophys. Astrophys. Fluid Dyn.*, **26**, 85–105.

— 1991: Two- and three-dimensional parametric instabilities in finite amplitude internal gravity waves. *Geophys. Astrophys. Fluid Dyn.*, **61**, 1–25.

Kwasniok, F. and G. Schmitz, 2003: Radiating instabilities of internal inertio-gravity waves. *J. Atmos. Sci.*, **60**, 1257–1269.

Landahl, M. T., 1980: A note on an algebraic instability of inviscid parallel shear flows. *J. Fluid Mech.*, **98**, 243–251.

Lelong, M. P. and T. J. Dunkerton, 1998a: Inertia-gravity wave breaking in three dimensions. Part I: Convectively stable waves. *J. Atmos. Sci.*, **55**, 2473–2488.

— 1998b: Inertia-gravity wave breaking in three dimensions. Part II: Convectively unstable waves. *J. Atmos. Sci.*, **55**, 2489–2501.

Lindzen, R. S., 1981: Turbulence and stress owing to gravity wave and tidal breakdown. *J. Geophys. Res.*, **86**, 9707–9714.

Lombard, P. N. and J. R. Riley, 1996: Instability and breakdown of internal gravity waves. I. Linear stability analysis. *Phys. Fluids*, **8**, 3271–3287.

Lübken, F.-J., 1997: Seasonal variation of turbulent energy dissipation rates at high latitudes as determined by in situ measurements of neutral density fluctuations. *J. Geophys. Res.*, **102**, 13441–13456.

Mied, R. P., 1976: The occurrence of parametric instabilities in finite amplitude internal gravity waves. *J. Fluid Mech.*, **78**, 763–784.

Miles, J. W., 1961: On the stability of heterogeneous shear flows. *J. Fluid Mech.*, **10**, 496–508.

Miyazaki, T. and K. Adachi, 1998: Short-wavelength instabilities of waves in rotating stratified fluids. *Phys. Fluids*, **10**, 3168–3177.

Moffat, H. K., 1967: The interaction of turbulence with strong shear. *Atmospheric Turbulence and Radio Wave Propagation*, A. M. Yaglom and V. I. Tatarskii, eds., Nauka, 139–161.

Müllemann, A., M. Rapp, and F.-J. Lübken, 2003: Morphology of turbulence in the polar summer mesopause region during the MIDAS/SOLSTICE campaign 2001. *Adv. Space Res.*, **31**, 2069–2074.

Orr, W. M., 1907: The stability or instability of the steady motions of a perfect liquid and of a viscous liquid. Part I: A perfect liquid. *Proc. Roy. Irish Acad.*, **27A**, 9–68.

Sonmor, L. J. and G. P. Klaassen, 1997: Toward a unified theory of gravity wave stability. *J. Atmos. Sci.*, **54**, 2655–2680.

Trefethen, L. N., A. E. Trefethen, S. C. Reddy, and T. A. Driscoll, 1993: Hydrodynamic stability without eigenvalues. *Science*, **261**, 578–584.

Winters, K. B. and E. A. D'Asaro, 1994: Three-dimensional wave instability near a critical level. *J. Fluid Mech.*, **272**, 255–284.

Yau, K.-H., G. P. Klaassen, and L. J. Sonmor, 2004: Principal instabilities of large amplitude inertio-gravity waves. *Phys. Fluids*, **16**, 936–951.

Yuan, L. and D. C. Fritts, 1989: Influence of a mean shear on the dynamical instability of an inertio-gravity wave. *J. Atmos. Sci.*, **46**, 2562–2568.

List of Figures

1 The rotated and translated coordinate system for the simplest representation of a gravity wave. The (orthogonal) ξ- and ϕ-axes lie in the $x - z$ plane. The y-axis points vertically into that plane. The new coordinate system moves with the phase velocity **c** of the gravity wave, rendering the latter stationary. 39

2 The budget for the exchange between the gravity-wave-phase averaged available potential energy A and kinetic energy K of the "horizontal" mean (denoted by an overbar, "vertical" meaning parallel to the direction of the gravity-wave wave vector) and the deviations from this mean (the eddies, denoted by a prime). For an explanation of the contributing terms see the main text. 40

3 For the statically unstable IGW ($a = 1.2$) at $(\Theta, \Lambda) = (89.5°, 6\mathrm{km})$, the initial perturbation energy density of the leading NMs and SVs at azimuthal angles $\alpha = 0, 90°$, normalized by the spatially independent energy density $\overline{E}$ of the IGW. All four perturbations have a local peak energy density $\max_{x_\parallel,\phi} e' = 10^{-3}\overline{E}$. 41

4 For the statically unstable IGW ($a = 1.2$) at $(\Theta, \Lambda) = (89.5°, 6\mathrm{km})$, perturbed by the leading NMs or SVs (optimization time $\tau = 300\mathrm{s}$) at azimuthal angles $\alpha = 0, 90°$ with an initial local peak energy density $\max_{x_\parallel,\phi} e' = 10^{-3}\overline{E}$ (see also Fig. 3), the time dependent energy in the horizontal mean, normalized by the initial value. 42

5 From the initial time span $0 \leq t \leq 10\tau$ of the integrations shown in Fig. 4 (left and right column for $\alpha = 0°$ and $90°$, top and bottom row for SV and NM perturbation), the time development of the instantaneous amplification-rate decomposition. 43

6 From the initial time span $0 \leq t \leq 20\tau$ of the integrations shown in Figs. 4 and 5, the time development of the dependence of the eddy energy on the IGW phase. All plots show normalized values $E'/\overline{E}(t=0)$. The shading scale in all four panels is identical. The contour interval is 0.1, starting at 0.1. 44

7 From the integration of the statically unstable IGW ($a = 1.2$) after a perturbation by its leading SV at $\alpha = 0°$, from between (from left to right) $t = \tau$ and $t = 2\tau$ in steps of 0.2τ, the instantaneous IGW-phase-dependent amplification-rate contribution $\gamma_\perp$ (fat black line) from eddy fluxes $\overline{v'_\perp u'_\phi}$ (normalized negative, thin black line) of $v_\perp$ against the phase-gradient in the horizontal-mean $\overline{v}_\perp$ (grey line). All quantities have been re-scaled to make them fit into one graph. Only the relevant phase range $0.6 \leq \phi/2\pi \leq 0.9$ is shown. 45

8 From the integration of the statically unstable IGW ($a = 1.2$) after a perturbation by its leading SV at $\alpha = 90°$, the time dependence of $\gamma_\perp$ (top panel, contour interval $5 \cdot 10^{-3}\mathrm{s}^{-1}$) and its contributing factors, i.e. the normalized counter-gradient flux $-\overline{u'_\phi v'_\perp}/\langle 2E' \rangle$ (middle, contour interval 0.1) and the phase-gradient $k\partial\overline{v}_\perp/\partial\phi$(bottom, contour interval $2 \cdot 10^{-2}\mathrm{s}^{-1}$). In all panels the negative values are indicated by dashed contours and shading, and the zero contour has not been drawn. Only the phase range $0.5 \leq \phi/2\pi \leq 1$ is shown. 46

9 From the integration of the statically unstable IGW ($a = 1.2$) after a perturbation by its leading NM at $\alpha = 90°$, the time dependence of the four eddy energy densities $K'_\parallel$, $K'_\perp$, K'_ϕ, and A'. Shown are relative values with respect to the initial IGW energy density. The shading scale in all four panels is the same. The contour indicates regions where the relative energy density is larger than 0.1. 47

10 For the statically and dynamically stable IGW ($a = 0.87$, no unstable NM) at $(\Theta, \Lambda) = (89.5°, 6\mathrm{km})$, the initial perturbation energy density of the leading SVs at azimuthal angles $\alpha = 0, 90°$ for the optimization times $\tau = 5\mathrm{min}, 30\mathrm{min}$, normalized by the spatially independent energy density $\overline{E}$ of the IGW. All four perturbations have a local peak energy density $\max_{x_\parallel,\phi} e' = 10^{-1}\overline{E}$. 48

11 For the statically and dynamically stable IGW ($a = 0.87$, no unstable NM) at $(\Theta, \Lambda) = (89.5°, 6\mathrm{km})$, the time dependence of the eddy energy $\langle E' \rangle$, normalized by the initial IGW energy, from integrations after a perturbation by one of the leading SVs at azimuthal angles $\alpha = 0, 90°$ (left and right column, respectively) for the optimization times $\tau = 5\mathrm{min}, 30\mathrm{min}$ (top and bottom row, respectively), and initial relative perturbation amplitudes $A^2_{\mathrm{SV}} = \max_{x_\parallel,\phi} e'/\overline{E} = 10^{-2}, 10^{-1}$, and 10^0. 49

12 As Fig. 11, but now showing the time dependence of the energy in the horizontal mean. 50

13 From the integrations of the leading SVs ($\alpha = 0, 90°$, $\tau = 5\mathrm{min}, 30\mathrm{min}$, in all cases the initial $A^2_{\mathrm{SV}} = 10^{-1}$) of the statically and dynamically stable IGW ($a = 0.87$, no unstable NM), the time development of the instantaneous amplification-rate decompositions. 51

14 From the integrations shown in Fig. 13, the time development of the dependence of the eddy energy on the IGW phase. All plots show normalized values $E'/\overline{E}(t = 0)$. The shading scale in all four panels is identical. The contour interval is 0.1, starting at 0.1. 52

15 From the integration of the statically and dynamically stable IGW ($a = 0.87$) after a perturbation by its leading SV at $(\tau, \alpha) = (5\mathrm{min}, 90°)$ with initial amplitude $A^2_{\mathrm{SV}} = 10^{-1}$, the time dependence of the four eddy energy densities $K'_{\parallel}$ (upper left panel), $K'_{\perp}$ (lower left), K'_{ϕ} (upper right), and A' (lower right). Shown are relative values with respect to the initial IGW energy density. The shading scale in all four panels is the same. The contour indicates regions where the relative energy density is larger than 0.1. 53

16 From the same integration as shown in Fig. 15, the time dependence of the IGW-phase dependent amplification-rate contribution γ_b (upper left panel, contour interval $0.01\mathrm{s}^{-1}$) from the buoyancy flux in phase direction (lower left panel, negative shown normalized by $2N\langle E'\rangle$, contour interval 0.2) against the corresponding gradient of the horizontal mean (upper right, normalized by N, contour interval $0.01\mathrm{s}^{-1}$). The lower right panel shows the difference $\gamma_b - \overline{b'u'_\phi}/\langle 2E'\rangle$ characterizing the net growth and decay of A' (contour interval $0.01\mathrm{s}^{-1}$). In all panels negative values are indicated by shading. 54

17 From the same integration as shown in Figs. 15 and 16, the time dependence of the IGW-phase dependent amplification-rate contribution $\gamma_{\parallel}$ (top panel, contour interval $0.002\mathrm{s}^{-1}$) from the flux of $u'_{\parallel}$ in phase direction (middle, negative shown normalized by $2\langle E'\rangle$, contour interval 0.1) against the corresponding gradient of the horizontal mean (bottom, contour interval $0.005\mathrm{s}^{-1}$). In all panels negative values are indicated by shading. 55

18 From the integration of the statically and dynamically stable IGW ($a = 0.87$) after a perturbation by its one of its leading SVs at $\tau = 5$min (left column $\alpha = 0°$, right column $\alpha = 90°$), the spatial dependence of $v_\perp$ at $t = \tau/6$ (top row), $t = \tau/3$ (middle) and $t = \tau/2$ (bottom). Only the phase range $0.5 \leq \phi/2\pi \leq 1$ is shown. The contour interval is 1m/s. The maximum value in the right column is between 20 and 21 m/s (all panels). Negative values are indicated by dashed contours. 56

19 As Fig. 18, but for $\tau = 30$min. 57

20 From the integration of the statically unstable IGW ($a = 1.2$) after a perturbation by its leading SVs or NMs at $\alpha = 0°, 90°$, the time dependence of the $\log_{10}[\epsilon'/\,(\mathrm{mW/kg})]$. The shading scale is the same in all four panels. Only values larger than 1 mW/kg are shown. The contour encloses regions with $\epsilon' > 10$mW/kg. 58

21 From the integration of the statically and dynamically stable IGW ($a = 0.87$) after a perturbation by the leading parallel SVs for $\tau = 5$min (top panel) or 30min (middle) or the leading transverse SV for $\tau = 30$min (bottom, initial amplitude in all cases $A^2_{\mathrm{SV}} = 10^{-1}$), the time-dependent ($0 \leq t \leq 2\tau$) eddy dissipation rate ϵ' in the phase range $\pi \leq \phi \leq 2\pi$. Shown is $\log_{10}\,[\epsilon'/\,(\mathrm{mW/kg})]$. The contour interval is 1, with the lowest contour also at 1. 59

22 As Fig. 21, but now from integrations of the leading transverse SV for $\tau = 5$min with initial amplitude $A^2_{\mathrm{SV}} = 10^{-1}$ (top panel) and 10^0 (bottom) between $0 \leq t \leq 5\tau$. 60

23 For $t = 40\tau$ in the integrations shown in Fig. 20, half the horizontally averaged spectra of the profiles of $u_\parallel$, $v_\perp$, u_ϕ, and b/N in ϕ-direction, and the sum, i.e. the spectrum of total energy. For better orientation the two lower panels also show a spectral slope $\propto m^{-5/3}$, where m is the wavenumber in ϕ-direction. . . 61

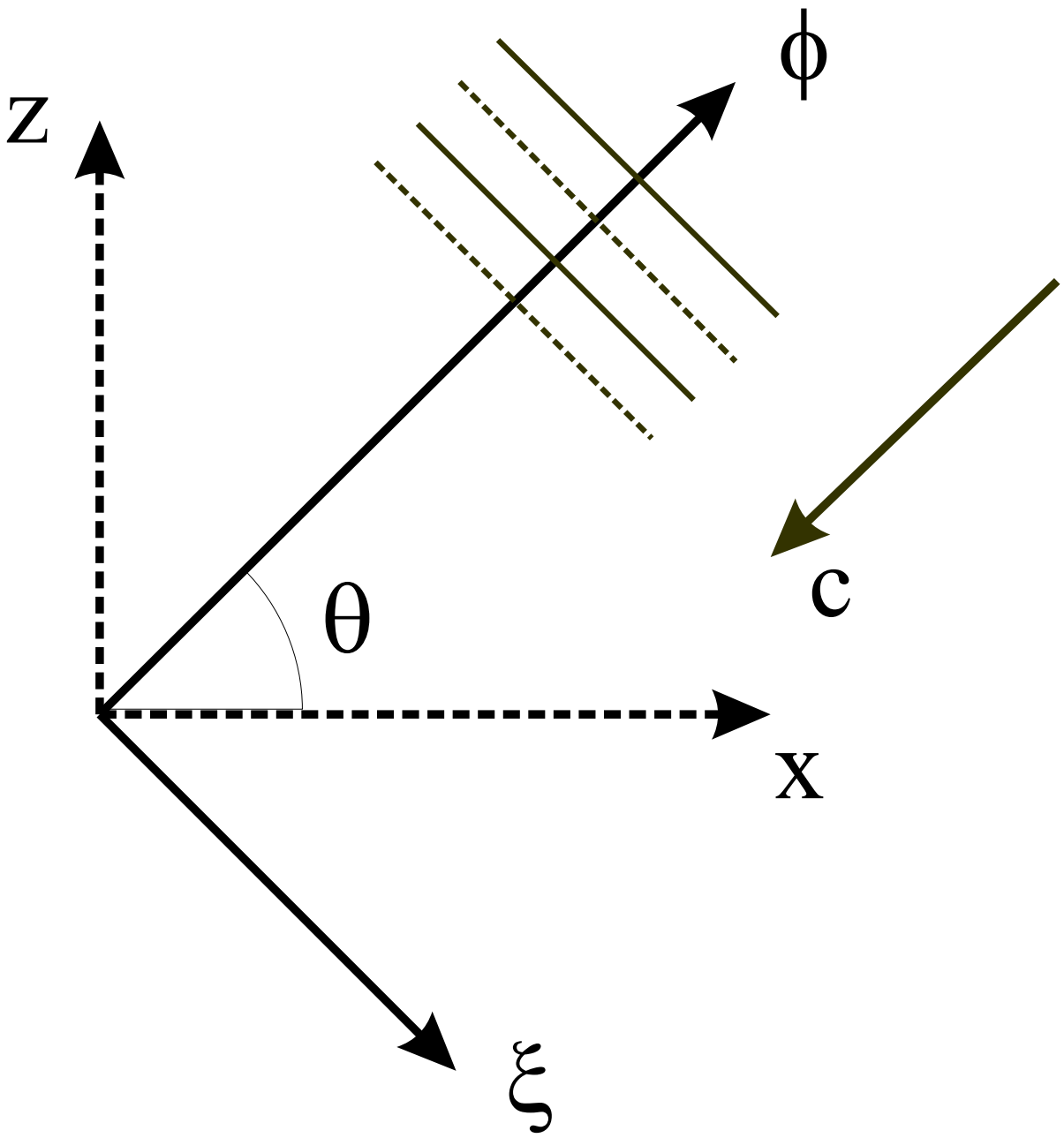

Figure 1: The rotated and translated coordinate system for the simplest representation of a gravity wave. The (orthogonal) ξ- and ϕ-axes lie in the $x-z$ plane. The y-axis points vertically into that plane. The new coordinate system moves with the phase velocity **c** of the gravity wave, rendering the latter stationary.

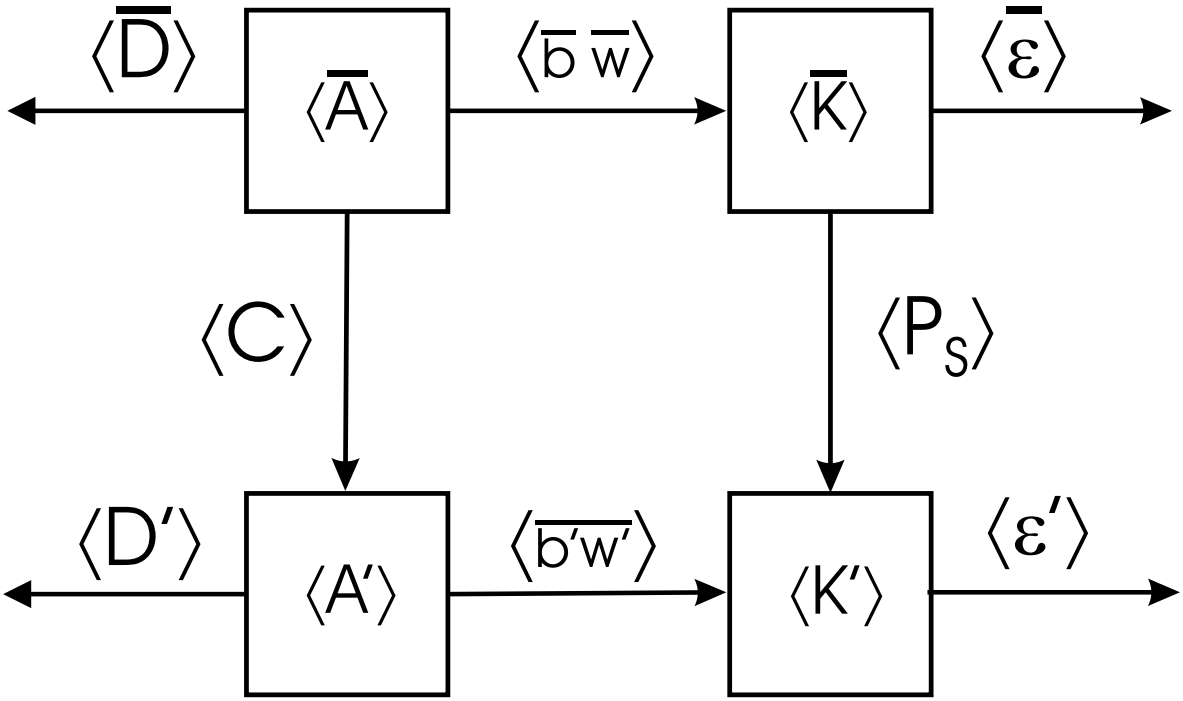

Figure 2: The budget for the exchange between the gravity-wave-phase averaged available potential energy A and kinetic energy K of the "horizontal" mean (denoted by an overbar, "vertical" meaning parallel to the direction of the gravity-wave wave vector) and the deviations from this mean (the eddies, denoted by a prime). For an explanation of the contributing terms see the main text.

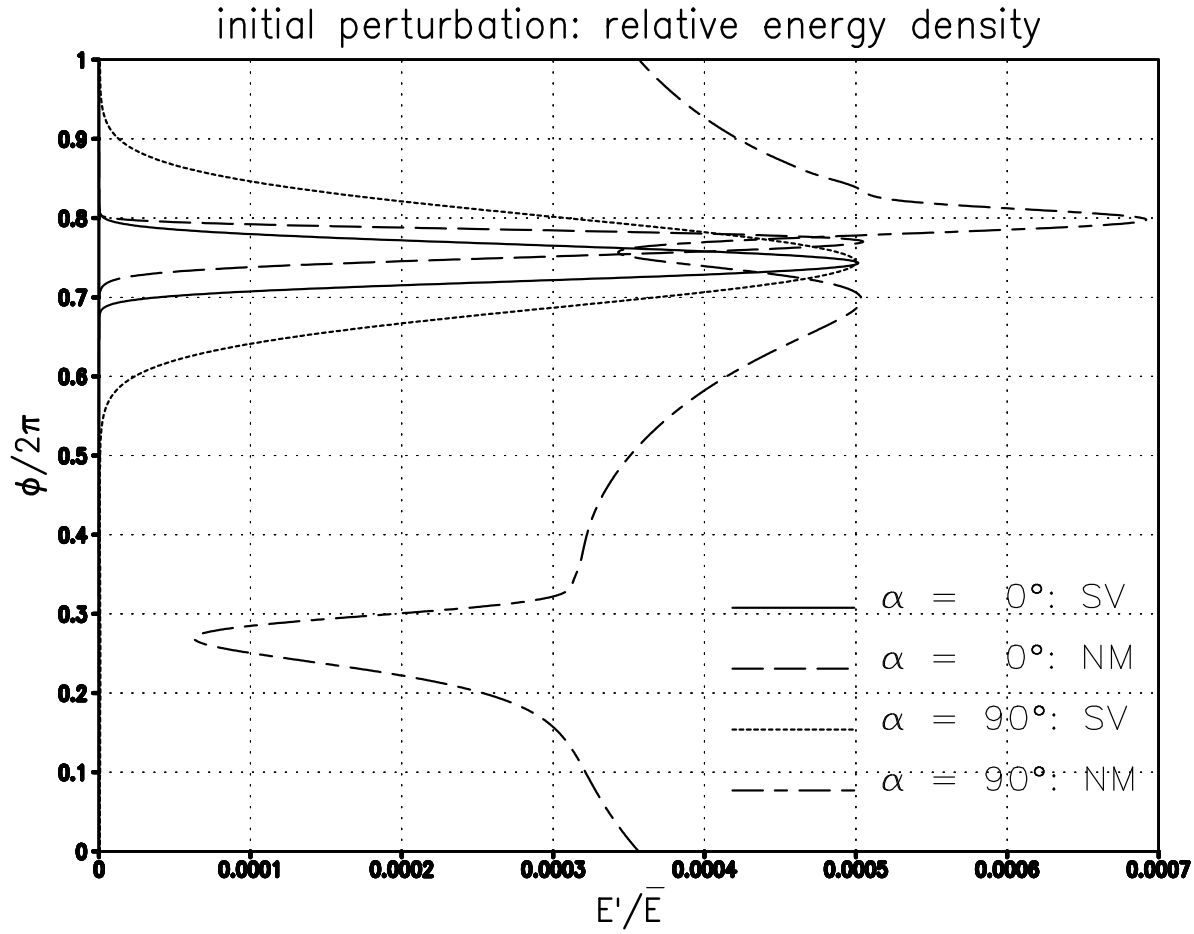

Figure 3: For the statically unstable IGW ($a = 1.2$) at $(\Theta, \Lambda) = (89.5°, 6\mathrm{km})$, the initial perturbation energy density of the leading NMs and SVs at azimuthal angles $\alpha = 0, 90°$, normalized by the spatially independent energy density $\overline{E}$ of the IGW. All four perturbations have a local peak energy density $\max_{x_\parallel,\phi} e' = 10^{-3}\overline{E}$.

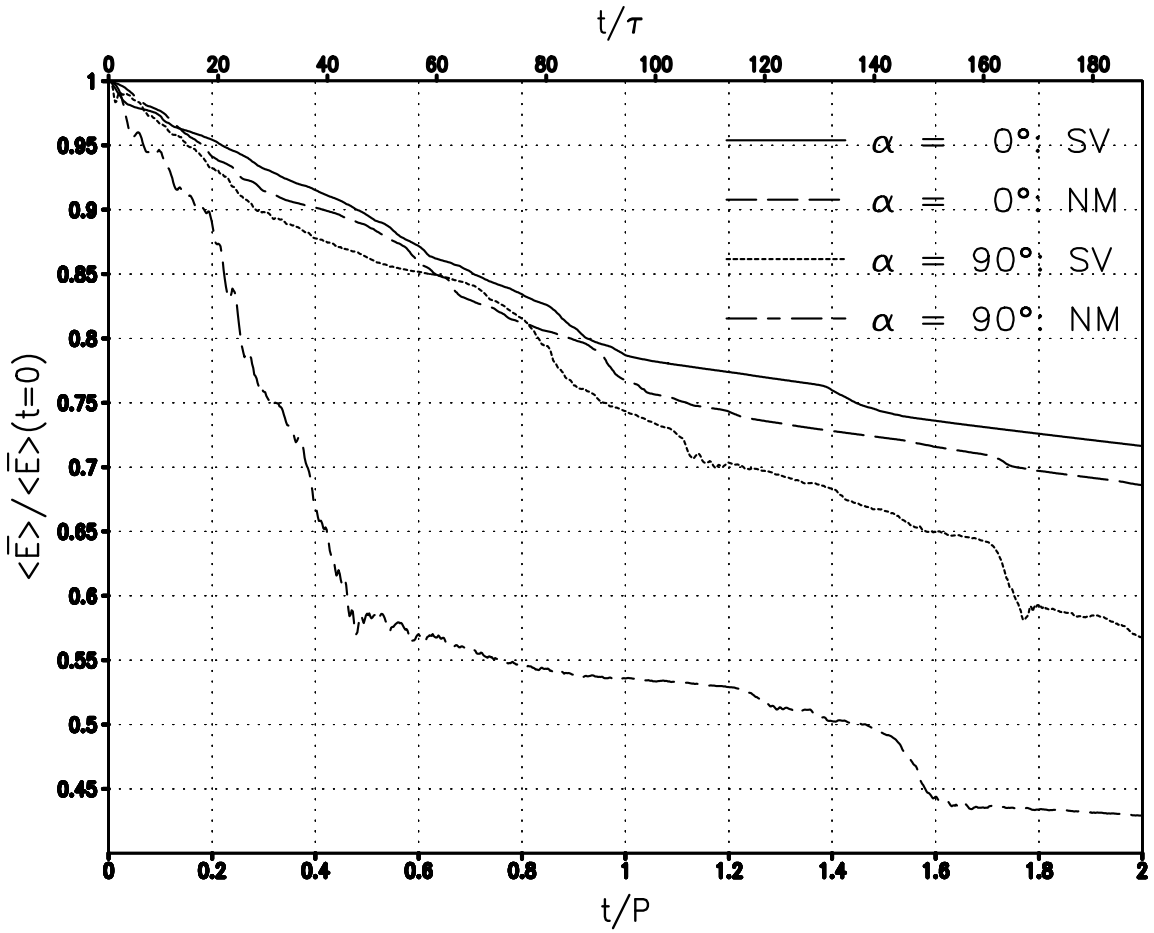

Figure 4: For the statically unstable IGW ($a = 1.2$) at $(\Theta, \Lambda) = (89.5°, 6\mathrm{km})$, perturbed by the leading NMs or SVs (optimization time $\tau = 300$s) at azimuthal angles $\alpha = 0, 90°$ with an initial local peak energy density $\max_{x_\parallel,\phi} e' = 10^{-3}\overline{E}$ (see also Fig. 3), the time dependent energy in the horizontal mean, normalized by the initial value.

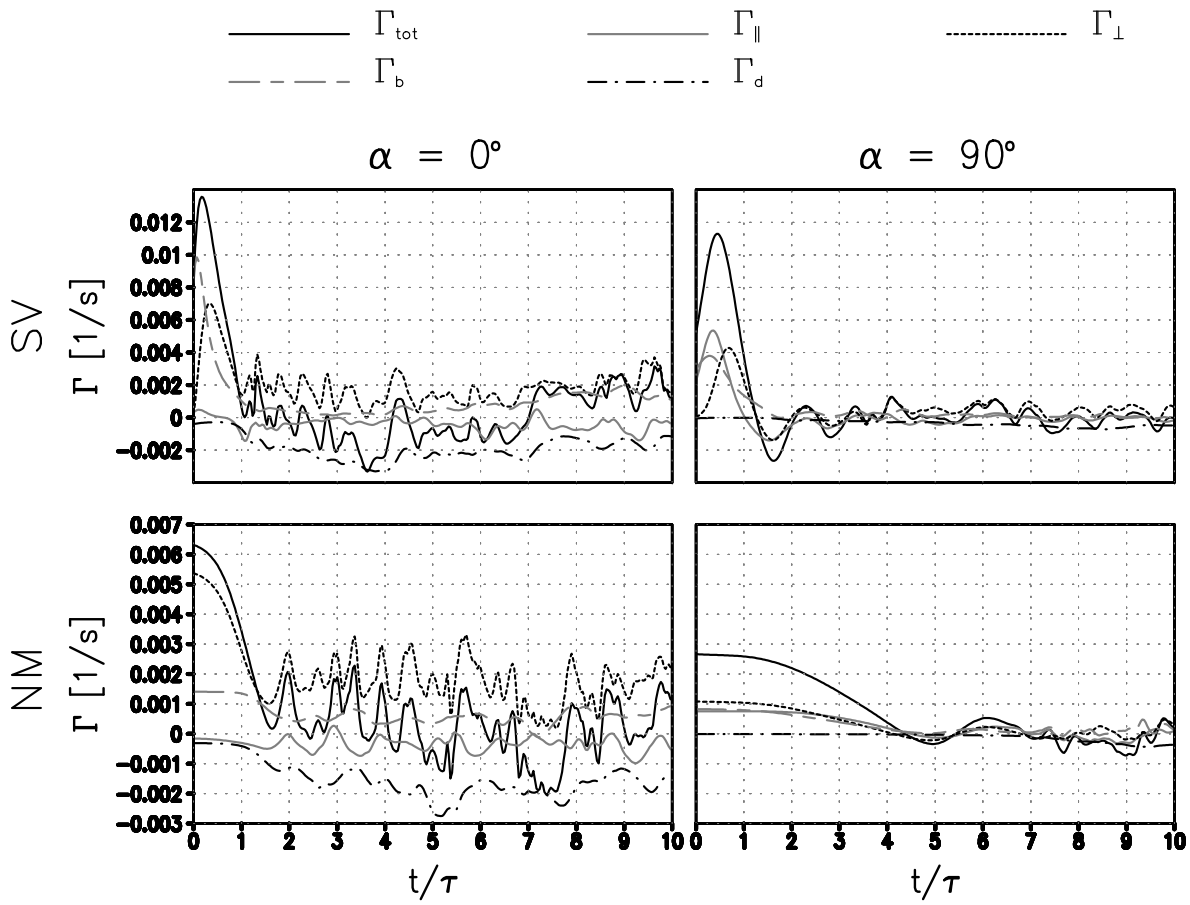

Figure 5: From the initial time span $0 \leq t \leq 10\tau$ of the integrations shown in Fig. 4 (left and right column for $\alpha = 0°$ and $90°$, top and bottom row for SV and NM perturbation), the time development of the instantaneous amplification-rate decomposition.

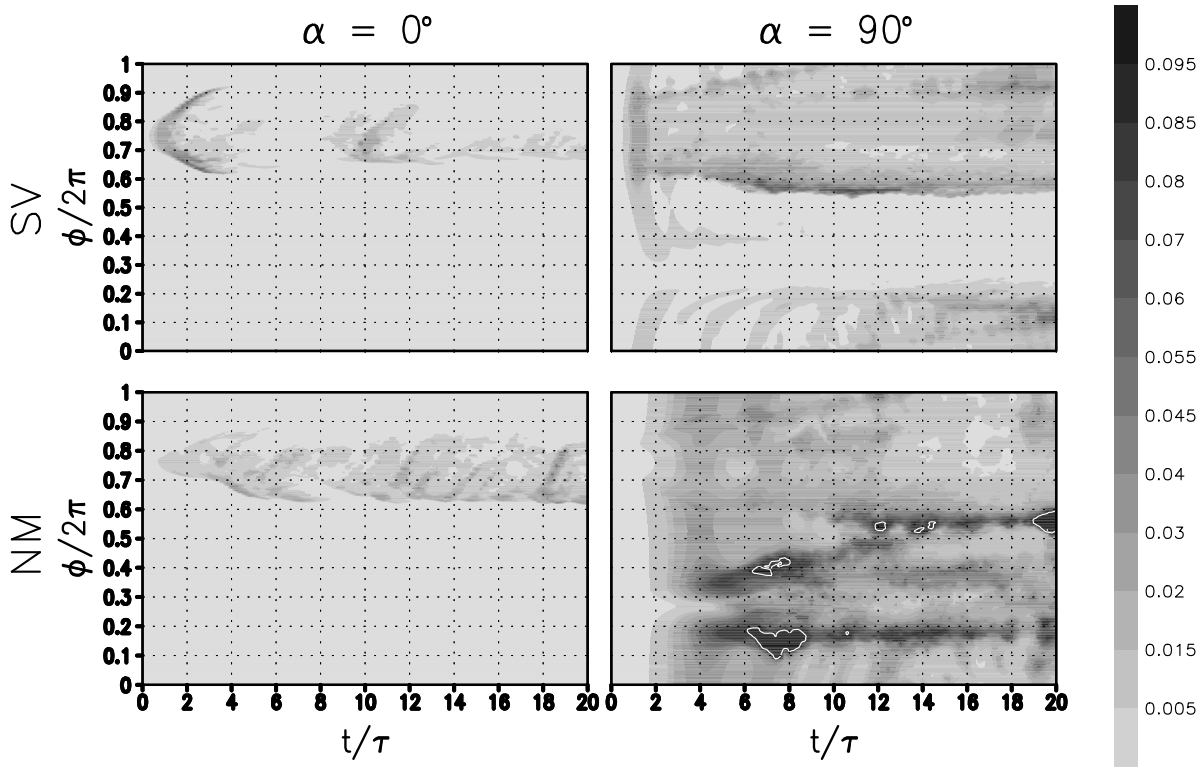

Figure 6: From the initial time span $0 \leq t \leq 20\tau$ of the integrations shown in Figs. 4 and 5, the time development of the dependence of the eddy energy on the IGW phase. All plots show normalized values $E'/\overline{E}(t=0)$. The shading scale in all four panels is identical. The contour interval is 0.1, starting at 0.1.

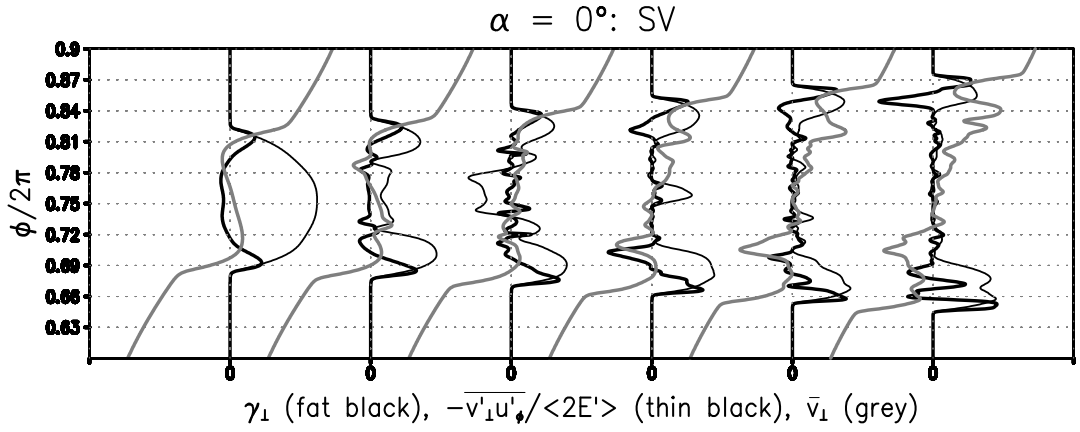

Figure 7: From the integration of the statically unstable IGW ($a = 1.2$) after a perturbation by its leading SV at $\alpha = 0°$, from between (from left to right) $t = \tau$ and $t = 2\tau$ in steps of 0.2τ, the instantaneous IGW-phase-dependent amplification-rate contribution $\gamma_\perp$ (fat black line) from eddy fluxes $\overline{v'_\perp u'_\phi}$ (normalized negative, thin black line) of $v_\perp$ against the phase-gradient in the horizontal-mean $\overline{v}_\perp$ (grey line). All quantities have been re-scaled to make them fit into one graph. Only the relevant phase range $0.6 \leq \phi/2\pi \leq 0.9$ is shown.

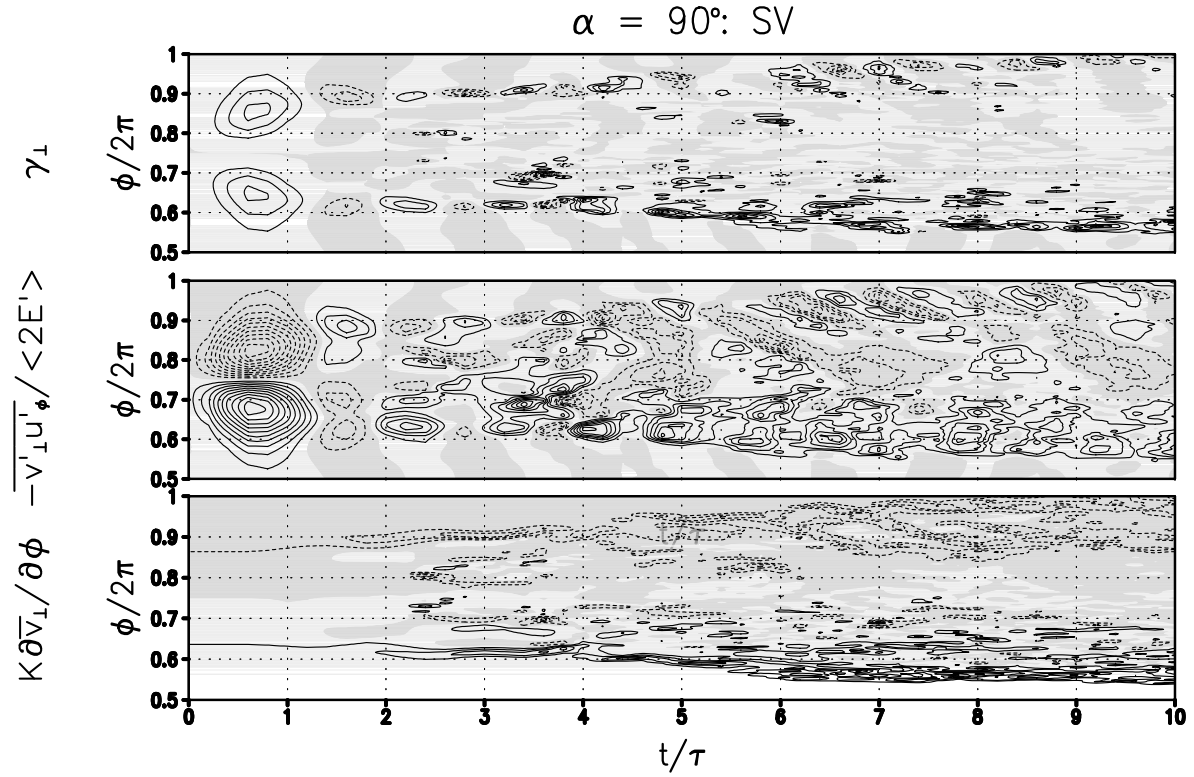

Figure 8: From the integration of the statically unstable IGW ($a = 1.2$) after a perturbation by its leading SV at $\alpha = 90°$, the time dependence of $\gamma_\perp$ (top panel, contour interval $5 \cdot 10^{-3}\mathrm{s}^{-1}$) and its contributing factors, i.e. the normalized counter-gradient flux $-\overline{u'_\phi v'_\perp}/\langle 2E' \rangle$ (middle, contour interval 0.1) and the phase-gradient $k\partial\overline{v}_\perp/\partial\phi$(bottom, contour interval $2 \cdot 10^{-2}\mathrm{s}^{-1}$). In all panels the negative values are indicated by dashed contours and shading, and the zero contour has not been drawn. Only the phase range $0.5 \leq \phi/2\pi \leq 1$ is shown.

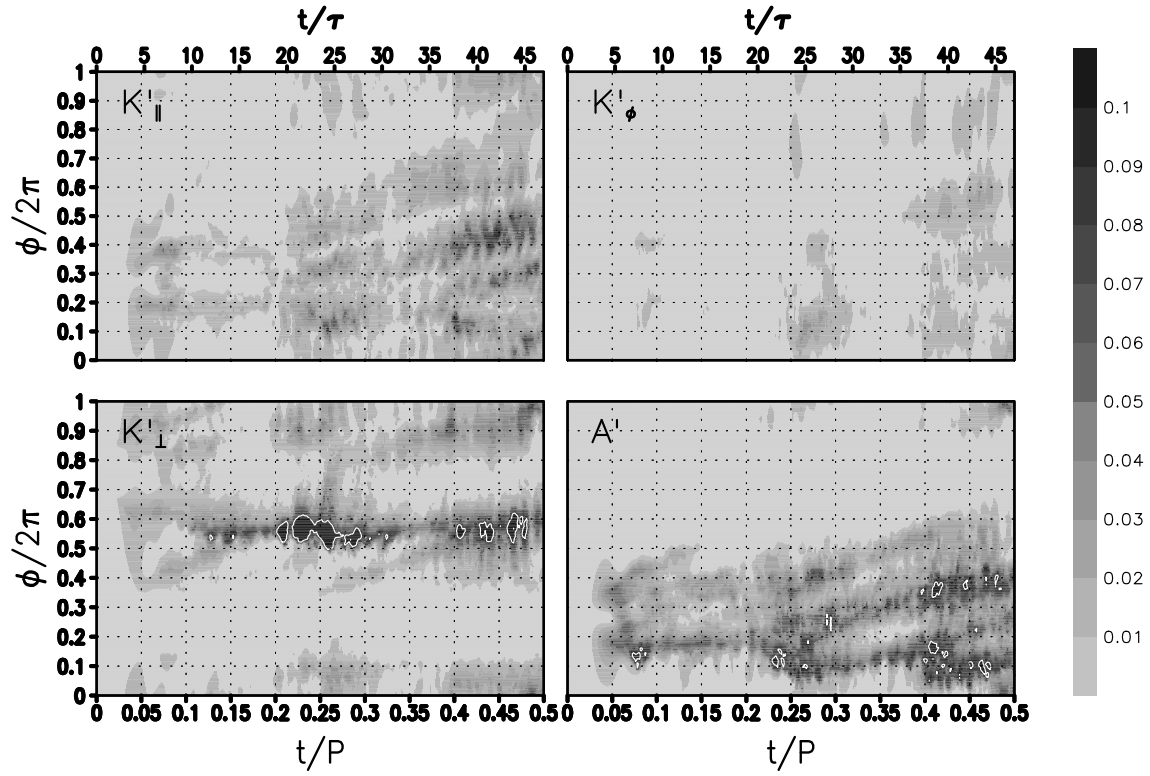

Figure 9: From the integration of the statically unstable IGW ($a = 1.2$) after a perturbation by its leading NM at $\alpha = 90°$, the time dependence of the four eddy energy densities $K'_{\parallel}$, $K'_{\perp}$, K'_{ϕ}, and A'. Shown are relative values with respect to the initial IGW energy density. The shading scale in all four panels is the same. The contour indicates regions where the relative energy density is larger than 0.1.

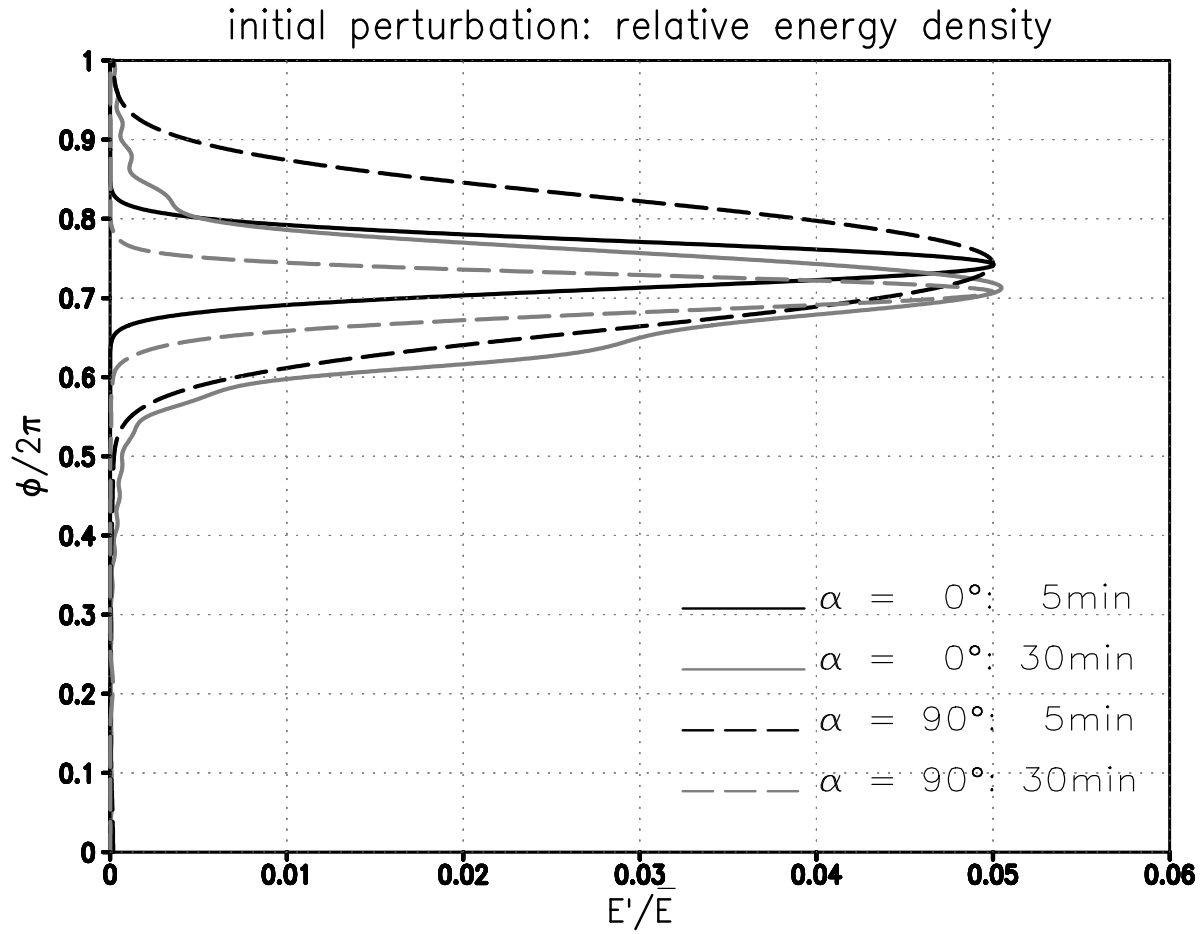

Figure 10: For the statically and dynamically stable IGW ($a = 0.87$, no unstable NM) at $(\Theta, \Lambda) = (89.5°, 6\mathrm{km})$, the initial perturbation energy density of the leading SVs at azimuthal angles $\alpha = 0, 90°$ for the optimization times $\tau = 5\mathrm{min}, 30\mathrm{min}$, normalized by the spatially independent energy density $\overline{E}$ of the IGW. All four perturbations have a local peak energy density $\max_{x_\parallel,\phi} e' = 10^{-1}\overline{E}$.

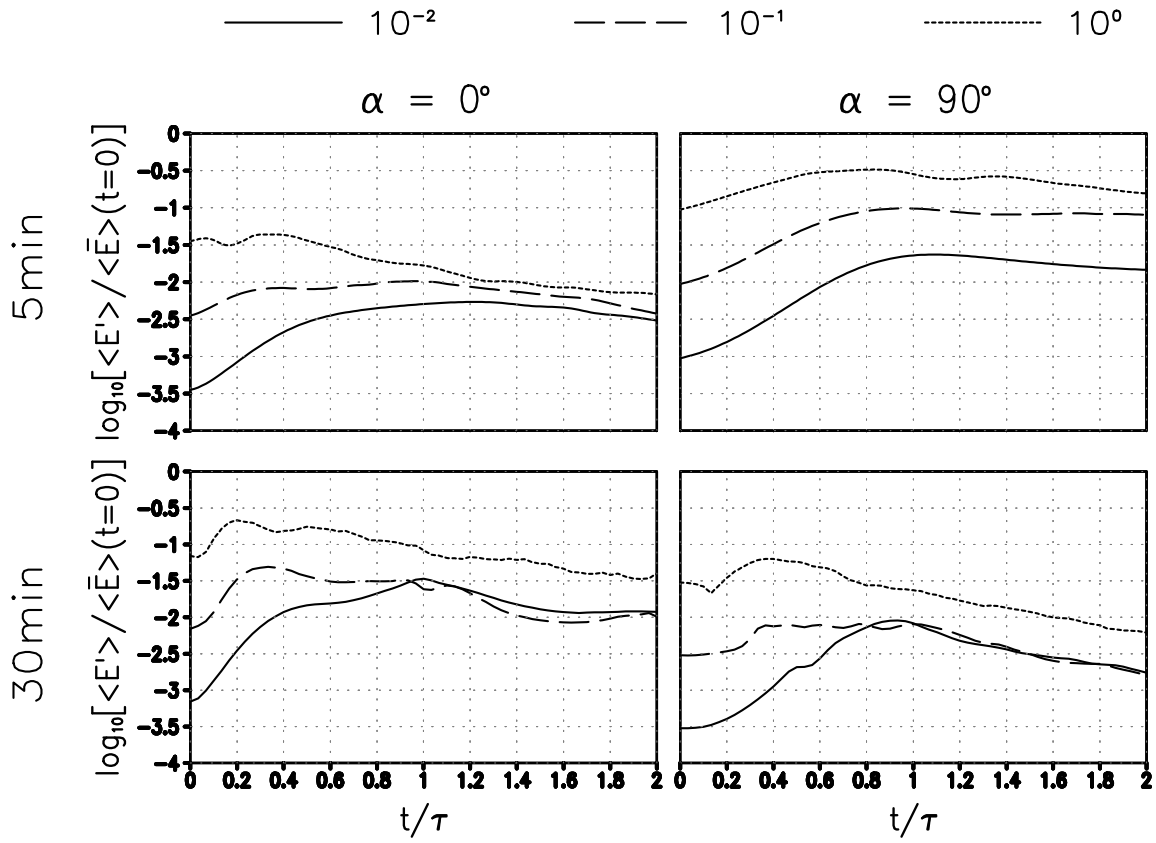

Figure 11: For the statically and dynamically stable IGW ($a = 0.87$, no unstable NM) at $(\Theta, \Lambda) = (89.5°, 6\mathrm{km})$, the time dependence of the eddy energy $\langle E' \rangle$, normalized by the initial IGW energy, from integrations after a perturbation by one of the leading SVs at azimuthal angles $\alpha = 0, 90°$ (left and right column, respectively) for the optimization times $\tau = 5\mathrm{min}, 30\mathrm{min}$ (top and bottom row, respectively), and initial relative perturbation amplitudes $A^2_{\mathrm{SV}} = \max_{x_\parallel, \phi} e'/\overline{E} = 10^{-2}, 10^{-1}$, and 10^0.

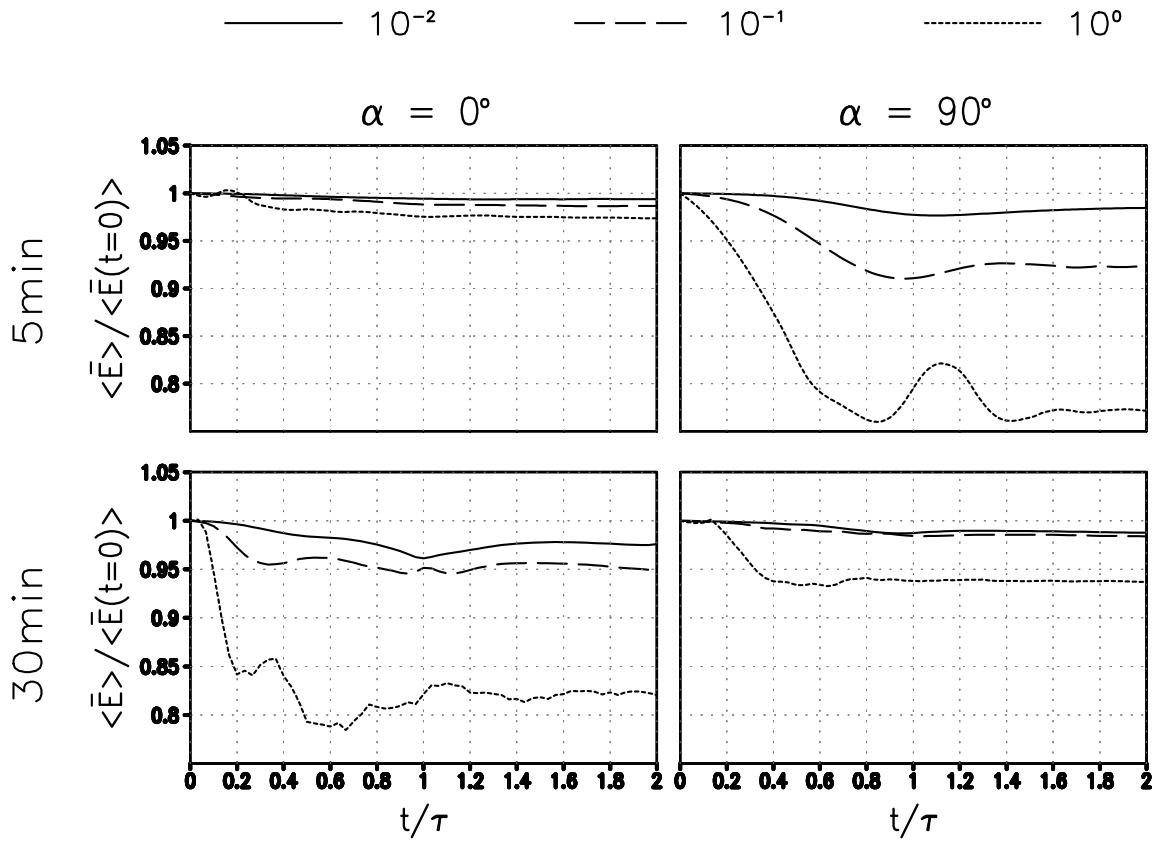

Figure 12: As Fig. 11, but now showing the time dependence of the energy in the horizontal mean.

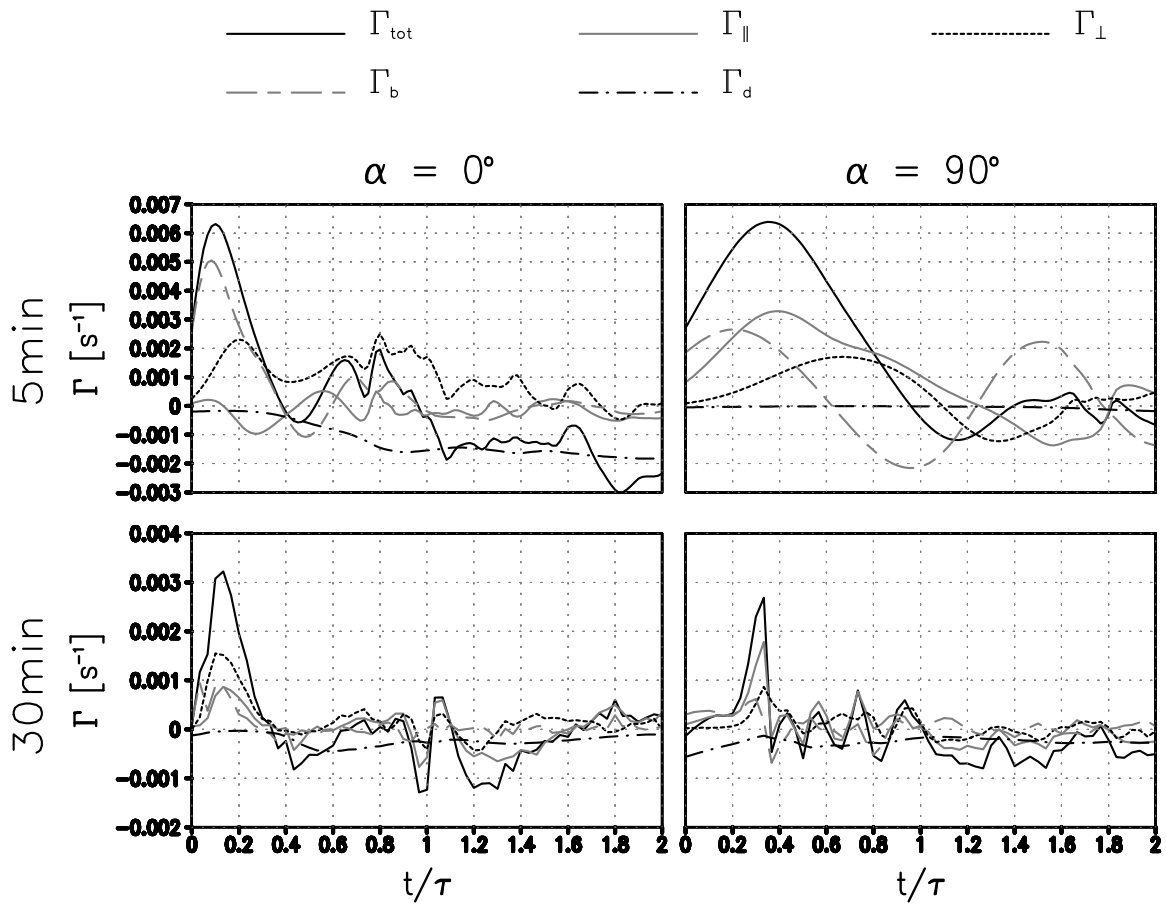

Figure 13: From the integrations of the leading SVs ($\alpha = 0, 90°$, $\tau = 5\mathrm{min}, 30\mathrm{min}$, in all cases the initial $A^2_{\mathrm{SV}} = 10^{-1}$) of the statically and dynamically stable IGW ($a = 0.87$, no unstable NM), the time development of the instantaneous amplification-rate decompositions.

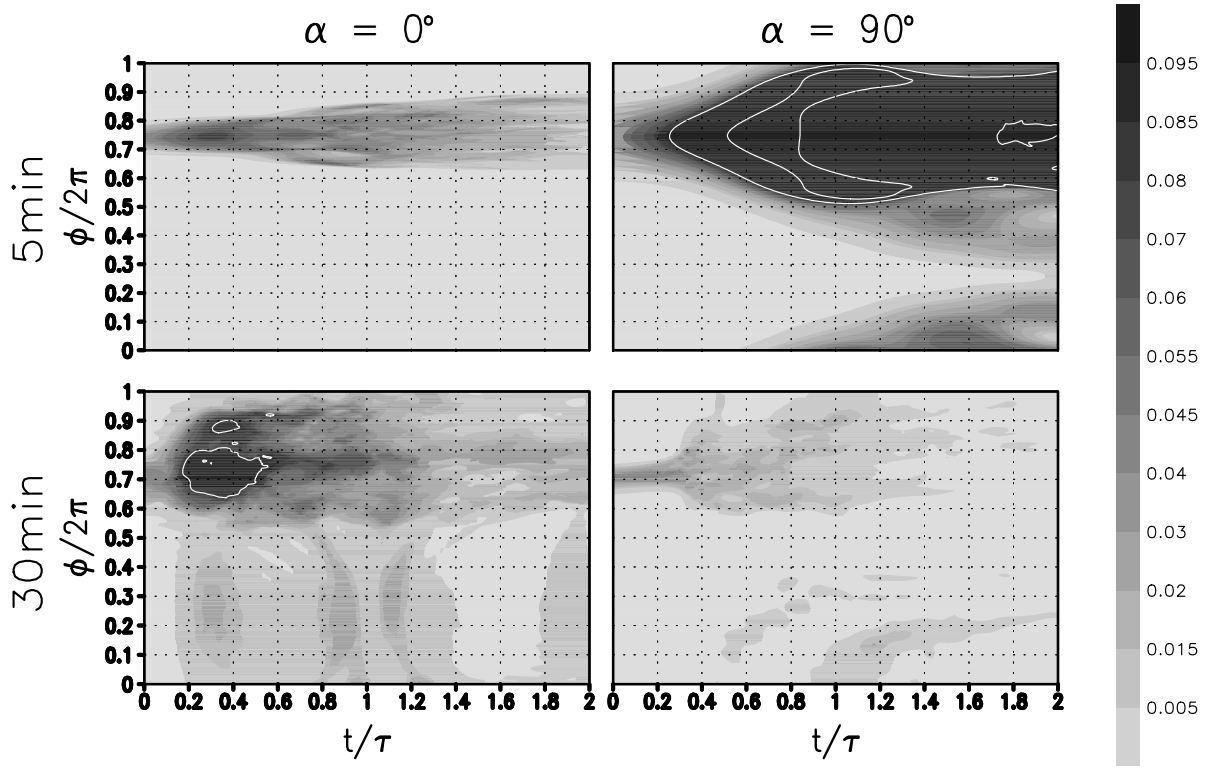

Figure 14: From the integrations shown in Fig. 13, the time development of the dependence of the eddy energy on the IGW phase. All plots show normalized values $E'/\overline{E}(t=0)$. The shading scale in all four panels is identical. The contour interval is 0.1, starting at 0.1.

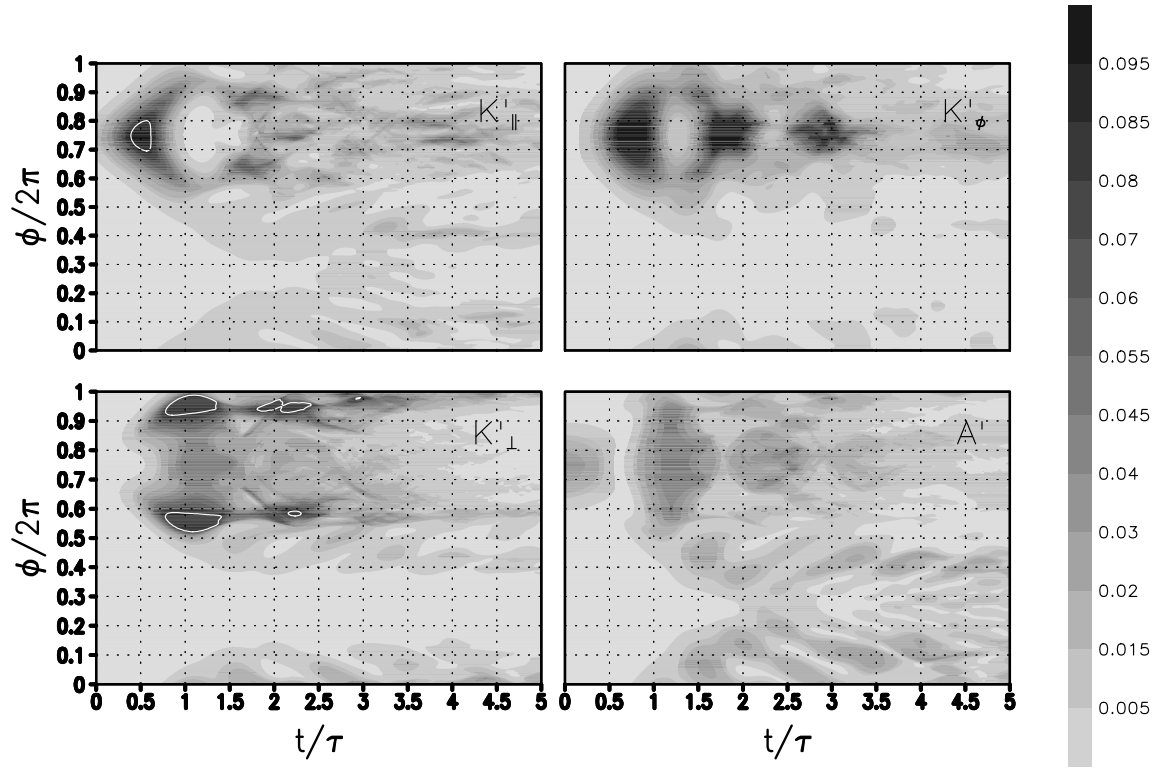

Figure 15: From the integration of the statically and dynamically stable IGW ($a = 0.87$) after a perturbation by its leading SV at $(\tau, \alpha) = (5\mathrm{min}, 90^\circ)$ with initial amplitude $A^2_{\mathrm{SV}} = 10^{-1}$, the time dependence of the four eddy energy densities $K'_\parallel$ (upper left panel), $K'_\perp$ (lower left), K'_ϕ (upper right), and A' (lower right). Shown are relative values with respect to the initial IGW energy density. The shading scale in all four panels is the same. The contour indicates regions where the relative energy density is larger than 0.1.

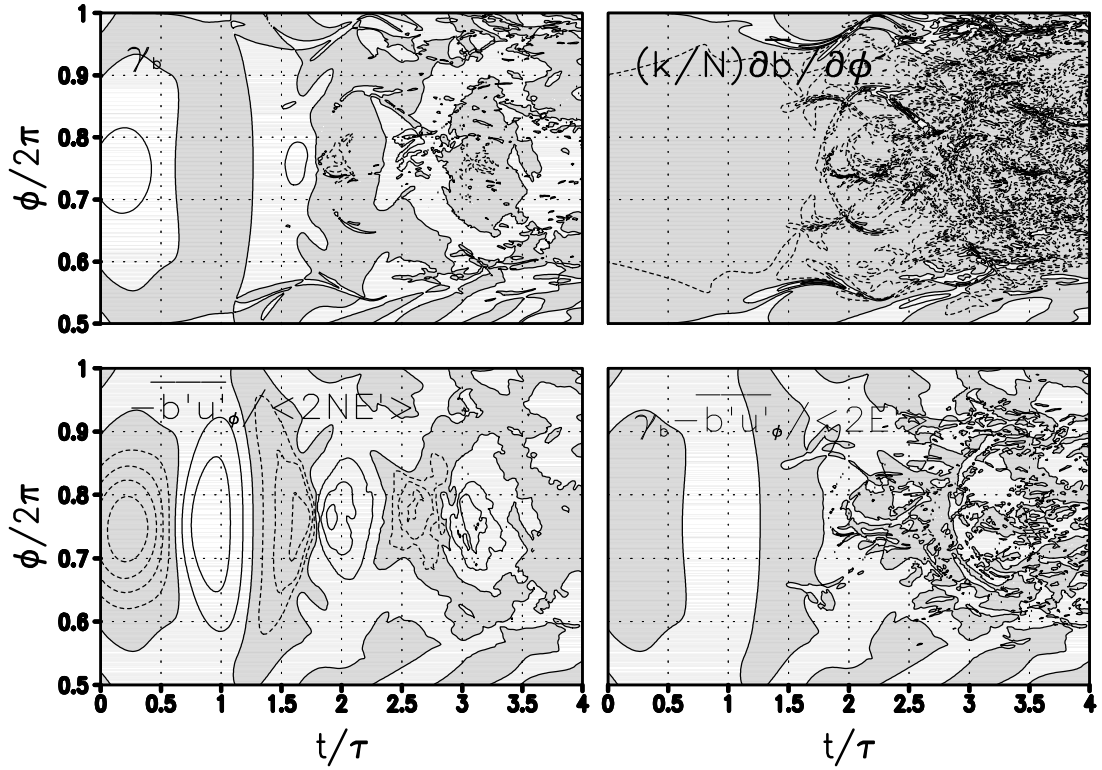

Figure 16: From the same integration as shown in Fig. 15, the time dependence of the IGW-phase dependent amplification-rate contribution γ_b (upper left panel, contour interval $0.01\mathrm{s}^{-1}$) from the buoyancy flux in phase direction (lower left panel, negative shown normalized by $2N\,\langle E'\rangle$, contour interval 0.2) against the corresponding gradient of the horizontal mean (upper right, normalized by N, contour interval $0.01\mathrm{s}^{-1}$). The lower right panel shows the difference $\gamma_b - \overline{b'u'_\phi}/\,\langle 2E'\rangle$ characterizing the net growth and decay of A' (contour interval $0.01\mathrm{s}^{-1}$). In all panels negative values are indicated by shading.

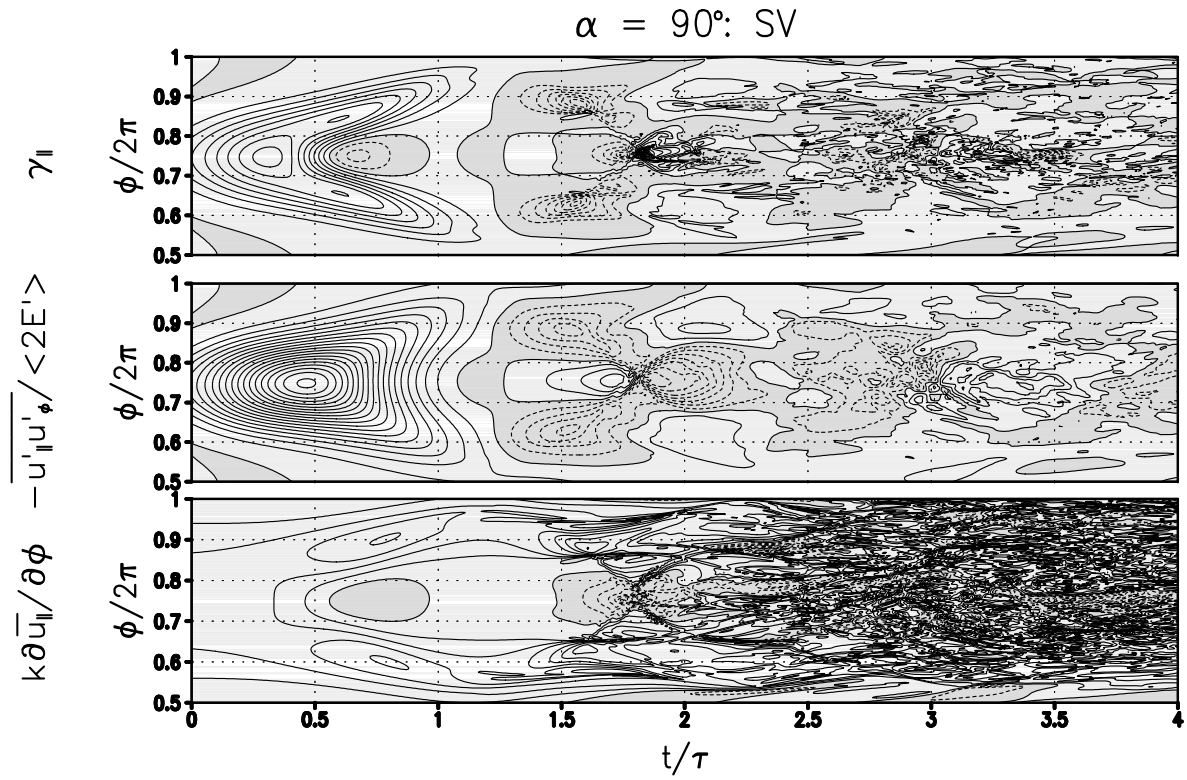

Figure 17: From the same integration as shown in Figs. 15 and 16, the time dependence of the IGW-phase dependent amplification-rate contribution $\gamma_{\|}$ (top panel, contour interval $0.002\mathrm{s}^{-1}$) from the flux of $u'_{\|}$ in phase direction (middle, negative shown normalized by $2\langle E'\rangle$, contour interval 0.1) against the corresponding gradient of the horizontal mean (bottom, contour interval $0.005\mathrm{s}^{-1}$). In all panels negative values are indicated by shading.

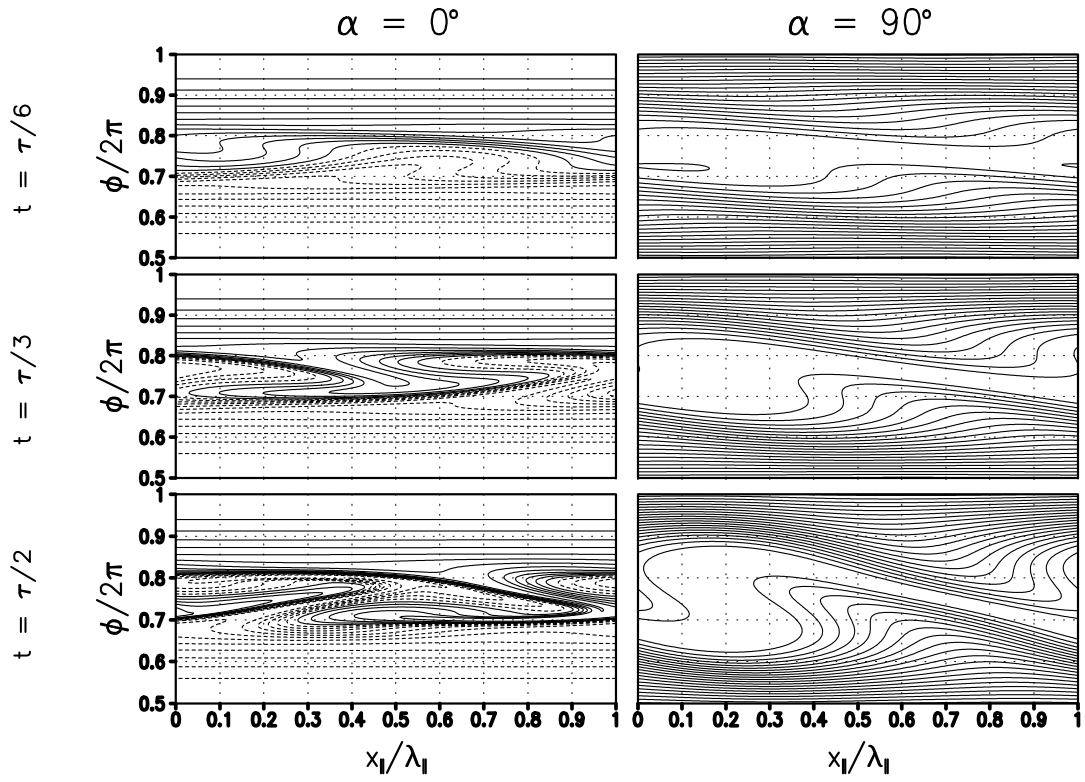

Figure 18: From the integration of the statically and dynamically stable IGW ($a = 0.87$) after a perturbation by its one of its leading SVs at $\tau = 5$min (left column $\alpha = 0°$, right column $\alpha = 90°$), the spatial dependence of $v_\perp$ at $t = \tau/6$ (top row), $t = \tau/3$ (middle) and $t = \tau/2$ (bottom). Only the phase range $0.5 \leq \phi/2\pi \leq 1$ is shown. The contour interval is 1m/s. The maximum value in the right column is between 20 and 21 m/s (all panels). Negative values are indicated by dashed contours.

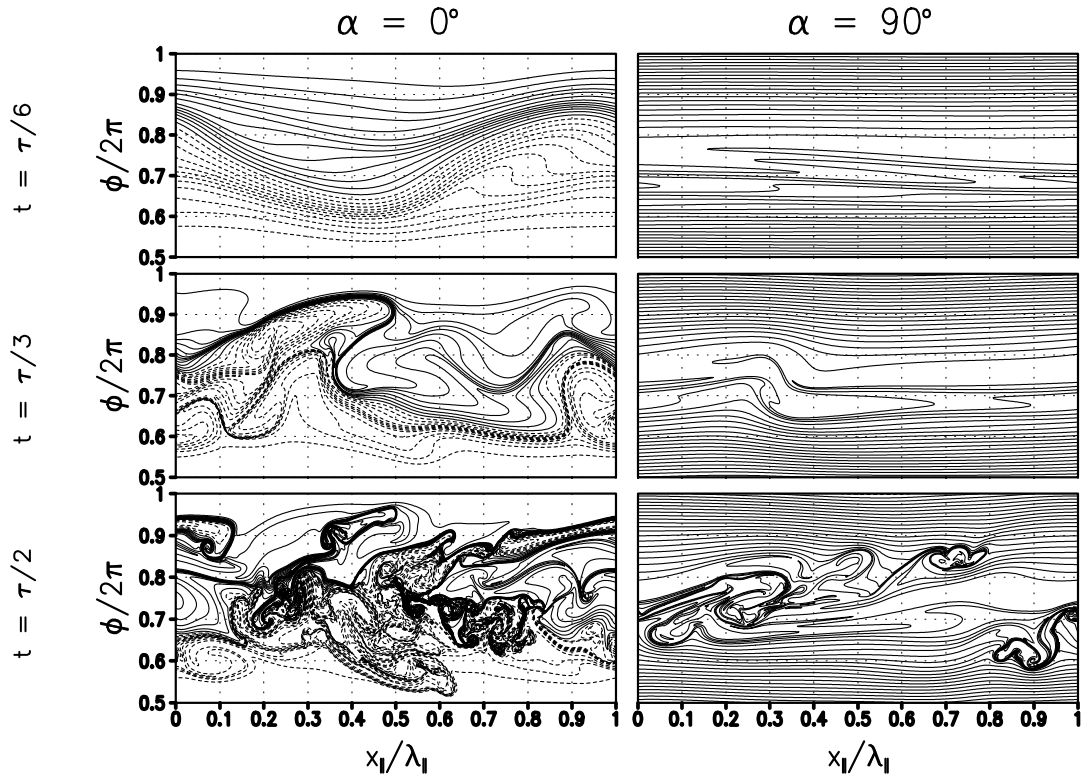

Figure 19: As Fig. 18, but for $\tau = 30$min.

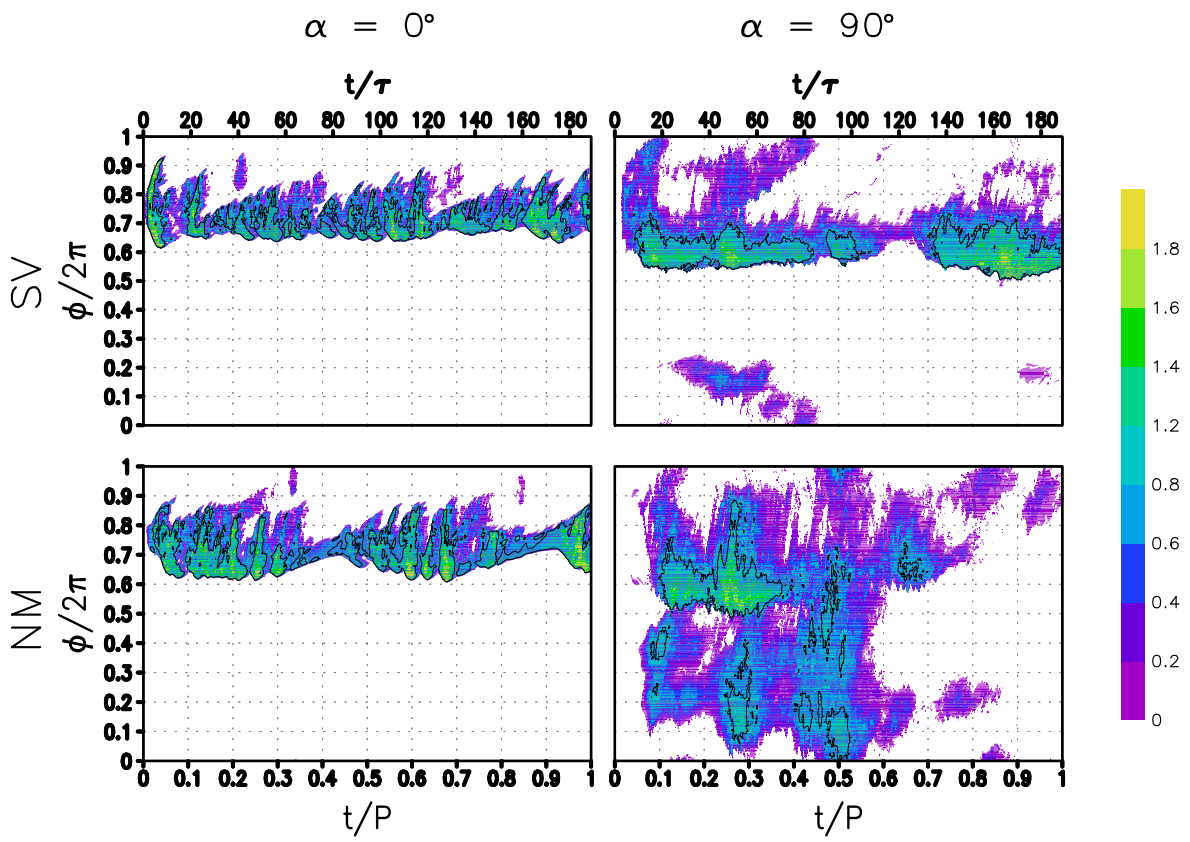

Figure 20: From the integration of the statically unstable IGW ($a = 1.2$) after a perturbation by its leading SVs or NMs at $\alpha = 0°, 90°$, the time dependence of the $\log_{10}[\epsilon'/\,(\mathrm{mW/kg})]$. The shading scale is the same in all four panels. Only values larger than 1 mW/kg are shown. The contour encloses regions with $\epsilon' > 10$mW/kg.

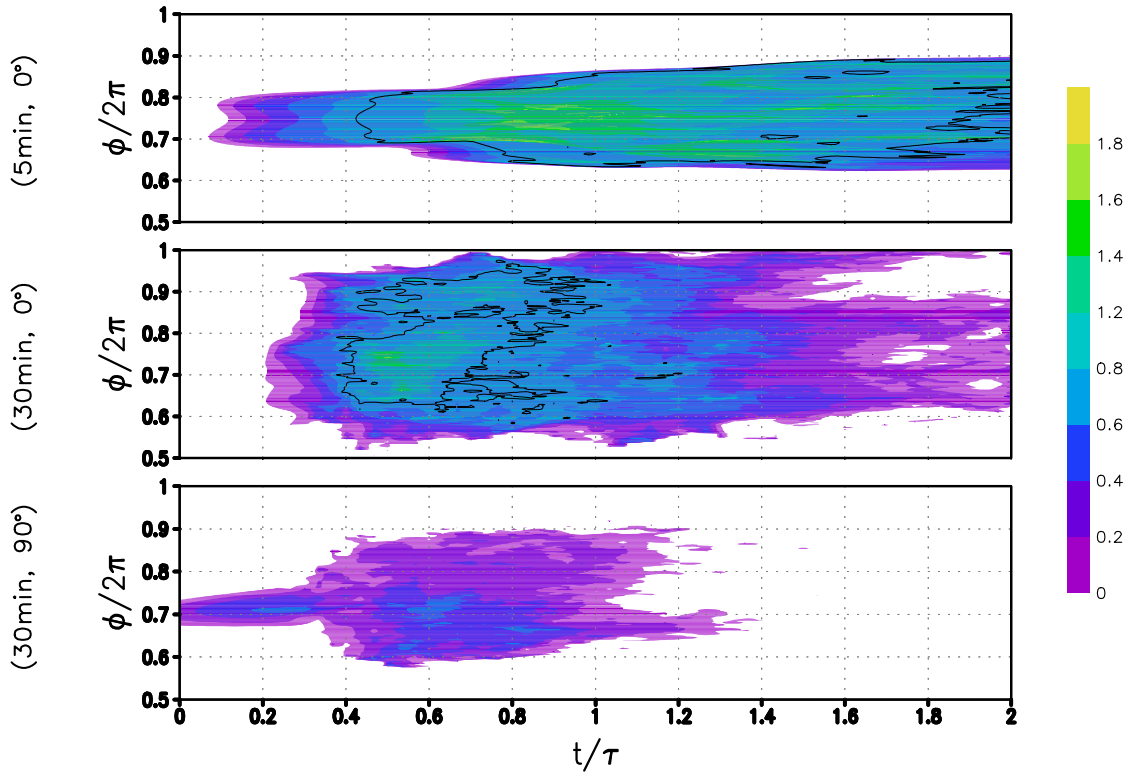

Figure 21: From the integration of the statically and dynamically stable IGW ($a = 0.87$) after a perturbation by the leading parallel SVs for $\tau = 5$min (top panel) or 30min (middle) or the leading transverse SV for $\tau = 30$min (bottom, initial amplitude in all cases $A^2_{\rm SV} = 10^{-1}$), the time-dependent ($0 \le t \le 2\tau$) eddy dissipation rate ϵ' in the phase range $\pi \le \phi \le 2\pi$. Shown is $\log_{10}[\epsilon'/\,({\rm mW/kg})]$. The contour interval is 1, with the lowest contour also at 1.

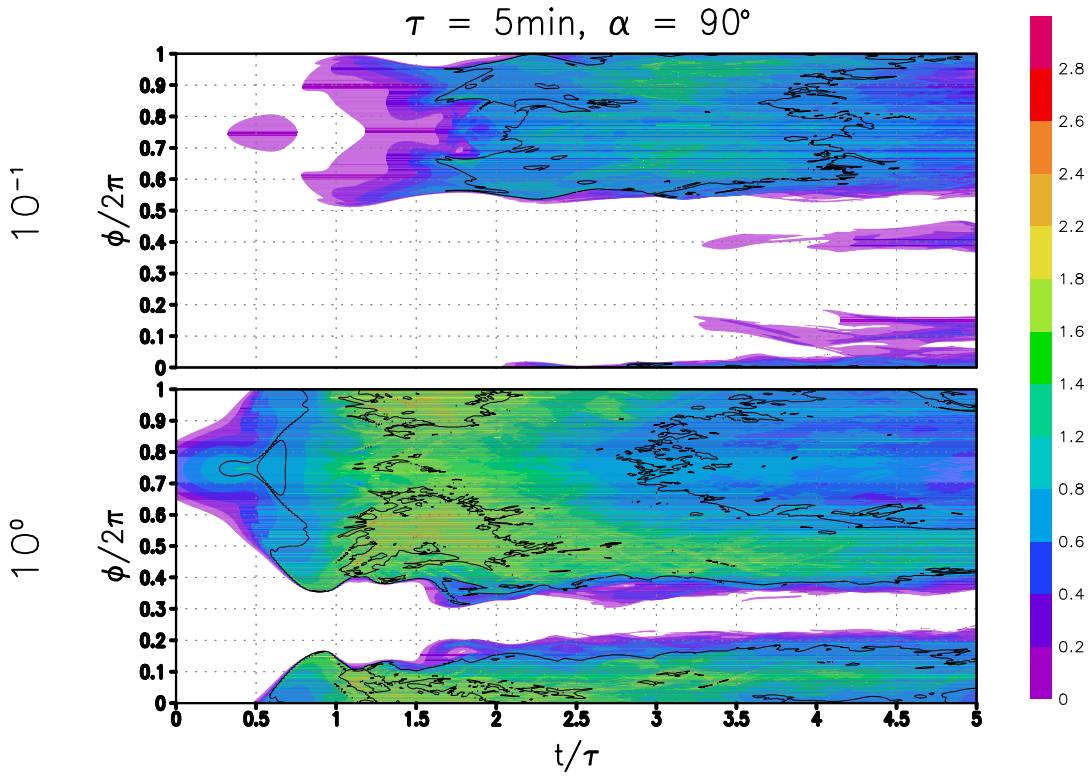

Figure 22: As Fig. 21, but now from integrations of the leading transverse SV for $\tau = 5$min with initial amplitude $A^2_{\rm SV} = 10^{-1}$ (top panel) and 10^0 (bottom) between $0 \leq t \leq 5\tau$.

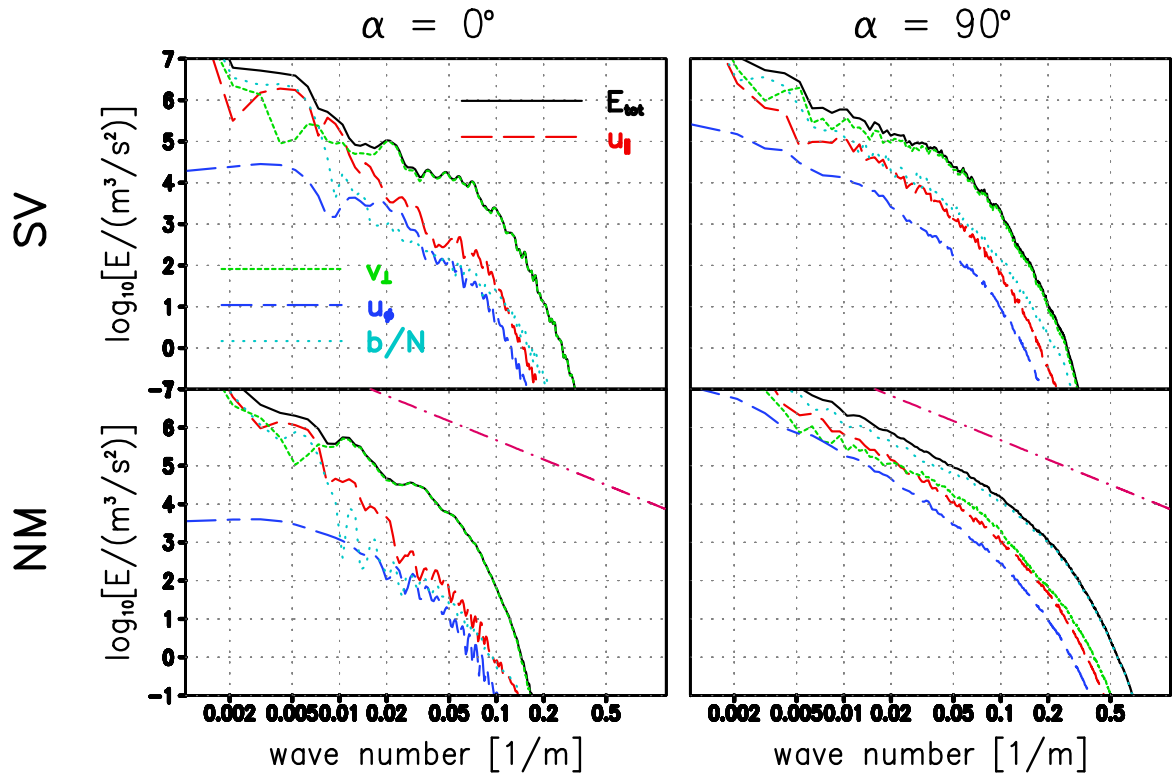

Figure 23: For $t = 40\tau$ in the integrations shown in Fig. 20, half the horizontally averaged spectra of the profiles of $u_{\|}$, $v_{\perp}$, u_{ϕ}, and b/N in ϕ-direction, and the sum, i.e. the spectrum of total energy. For better orientation the two lower panels also show a spectral slope $\propto m^{-5/3}$, where m is the wavenumber in ϕ-direction.

List of Tables

1 Model extent $\lambda_{\parallel}$ in the horizontal and Λ in IGW-phase direction, as well as the corresponding number of grid points $n_{\parallel}$ and n_{ϕ}, for all discussed integrations, of either leading SV (optimization time τ) or NM (azimuthal angle α), of an IGW with an amplitude a with respect to the overturning limit. Λ is also the IGW wavelength, while $\lambda_{\parallel}$ agrees with the horizontal wavelength of the respective perturbations. Θ is the inclination angle between the IGW wave vector and the horizontal. 63

$\Theta/^\circ$	a	Λ/km	perturbation type	τ/min	$\alpha/^\circ$	$\lambda_\parallel/\mathrm{km}$	$n_\parallel$	n_ϕ
89.5	1.20	6	SV	5	0	0.398	144	2304
89.5	1.20	6	SV	5	90	3.981	2304	2304
89.5	1.20	6	NM	–	0	0.501	288	2304
89.5	1.20	6	NM	–	90	7.943	4608	2304
89.5	0.87	6	SV	5	0	0.631	288	2304
89.5	0.87	6	SV	5	90	3.162	1152	2304
89.5	0.87	6	SV	30	0	7.943	4608	2304
89.5	0.87	6	SV	30	90	5.012	2304	2304

Table 1: Model extent $\lambda_\parallel$ in the horizontal and Λ in IGW-phase direction, as well as the corresponding number of grid points $n_\parallel$ and n_ϕ, for all discussed integrations, of either leading SV (optimization time τ) or NM (azimuthal angle α), of an IGW with an amplitude a with respect to the overturning limit. Λ is also the IGW wavelength, while $\lambda_\parallel$ agrees with the horizontal wavelength of the respective perturbations. Θ is the inclination angle between the IGW wave vector and the horizontal.